



HAL
open science

Numerical simulation of mass transfer dynamics in Taylor flows

Colin Butler, Emmanuel Cid, Anne-Marie Billet, Benjamin Lalanne

► **To cite this version:**

Colin Butler, Emmanuel Cid, Anne-Marie Billet, Benjamin Lalanne. Numerical simulation of mass transfer dynamics in Taylor flows. *International Journal of Heat and Mass Transfer*, 2021, 179, pp.121670. 10.1016/j.ijheatmasstransfer.2021.121670 . hal-03331976

HAL Id: hal-03331976

<https://hal.science/hal-03331976>

Submitted on 2 Sep 2021

HAL is a multi-disciplinary open access archive for the deposit and dissemination of scientific research documents, whether they are published or not. The documents may come from teaching and research institutions in France or abroad, or from public or private research centers.

L'archive ouverte pluridisciplinaire **HAL**, est destinée au dépôt et à la diffusion de documents scientifiques de niveau recherche, publiés ou non, émanant des établissements d'enseignement et de recherche français ou étrangers, des laboratoires publics ou privés.



Open Archive Toulouse Archive Ouverte

OATAO is an open access repository that collects the work of Toulouse researchers and makes it freely available over the web where possible

This is an author's version published in: <http://oatao.univ-toulouse.fr/28163>

Official URL :

<https://doi.org/10.1016/j.ijheatmasstransfer.2021.121670>

To cite this version:

Butler, Colin  and Cid, Emmanuel  and Billet, Anne-Marie  and Lalanne, Benjamin  *Numerical simulation of mass transfer dynamics in Taylor flows.* (2021) *International Journal of Heat and Mass Transfer*, 179. ISSN 0017-9310

Any correspondence concerning this service should be sent to the repository administrator: tech-oatao@listes-diff.inp-toulouse.fr

Numerical simulation of mass transfer dynamics in Taylor flows

Colin Butler^{a,b}, Emmanuel Cid^{a,b}, Anne-Marie Billet^{a,b}, Benjamin Lalanne^{a,b,*}

^aLaboratoire de Génie Chimique, CNRS & Université de Toulouse, France

^bFédération de recherche FERMAT, CNRS, Toulouse, France

ARTICLE INFO

Article history:

Received 22 January 2021

Revised 24 June 2021

Accepted 3 July 2021

Keywords:

Taylor flow

Bubbles

Direct numerical simulation

Level-Set method

Ghost fluid method

Mass transfer coefficient

Local transfer mechanisms

ABSTRACT

Direct Numerical Simulations of mass transfer within Taylor flows are carried out using the periodic unit-cell approach by means of the Level-Set method, under the axisymmetric assumption. The considered cases are based on the experimental study of Butler et al. [1] (absorption of gaseous species) for bubbles of Reynolds numbers $Re_b > 200$ and capillary numbers $Ca > 10^{-3}$. Firstly, the hydrodynamics of five cases are calculated up to steady state, after which the bubble shape, lubrication film thickness and velocity profiles are compared to experimental and theoretical results. Using these converged hydrodynamics, the transient mass transfer between the gas and liquid phases is then simulated, assuming no change in bubble volume. The Péclet number Pe is varied between 10 and 900 by changing the diffusion coefficient, allowing for new insight into local phenomena of mass transfer. In this way, the maximal transfer fluxes at the interface are observed to be (i) close to the stagnation point at the film entrance, and (ii) at the rear cap where the tangential velocity is greatest. As once as the mass transfer coefficient becomes constant, the fluxes across the part of the interface in contact with the film and around the bubble caps are each characterised by a local Sherwood number. The latter evolves by $\sqrt{Pe_{film}}$ across the film and is found to be predictable by a simple model when $Pe_{film} > 1$, where Pe_{film} is the film Péclet number. Concerning the caps, it evolves by \sqrt{Pe} but only in a finite range of Pe , contrary to the common assumption of similarity of transfer around the caps with that around a rising unconfined spherical bubble. Such local analyses could be further used in multizone models of mass transfer for Taylor flows. Finally, a correlation is proposed to scale the global Sherwood number Sh_∞ far from channel inlet, defined as a function of both a Péclet number Pe_R based on the relative velocity between the bubble and the two-phase flow, and the gas volume fraction in the unit cell. Its predictions are discussed against experimental results at much higher Péclet numbers, after showing that Sh_∞ is independent on the initial concentration distribution in the liquid (the latter being sensitive to the injection conditions in experiments).

1. Introduction

Gas-liquid Taylor flows, which consist of trains of bubbles separated by liquid slugs, with the bubbles being of comparable diameter to that of the tube, are commonly encountered in millimetric or microfluidic devices used as microreactors or monolithic chemical reactors. The existence of the Taylor flow regime depends on the ratio of superficial gas and liquid velocities [2], and it is a regime which is actively sought since it allows good controllability of the reacting system and promotes enhanced heat and mass transfer compared to other chemical reactors. Therefore, it is crucial to characterise the transfer dynamics between the gas and the

liquid phase, either in the presence or absence of chemical reaction.

For the case of physical absorption of concentrated gas in the surrounding liquid, resistance to transfer lies in the liquid phase. In a train of Taylor bubbles, mass transfer has been experimentally studied by several authors, based on either global measurements of the liquid concentration at inlet and outlet of the capillary tube [3–6], or, more recently, based on visualisation or measurement of the concentration field in the liquid slug [1,7,8]. However, the effective contributions from the different bubble zones in the whole transfer process is still under debate.

Most of the existing studies are dedicated to producing global correlations, either of the mass transfer coefficient $k_L a$ or the global Sherwood number Sh , but these correlations generally badly reproduce the influence of all the different parameters playing a role in the mass transfer dynamics, possibly due to the difficulty

* Corresponding author.

E-mail address: benjamin.lalanne@ensiacet.fr (B. Lalanne).

Nomenclature

Bo	Bond number (-)
C	local mass concentration (mg/L)
\bar{C}	volume average mass concentration in the liquid (mg/L)
C^*	mass saturation concentration (mg/L)
Ca	capillary number (-)
D	diffusion coefficient (m^2/s)
d	diameter (m)
g	acceleration due to gravity (m/s^2)
H	Heavyside function
J	mass transfer flux (mg/s)
j	diffusion flux density (mg/ m^2/s)
k	mass transfer coefficient (m/s)
L	length (m)
\mathbf{n}	normal vector
P	pressure (Pa)
Pe	Péclet number (-)
Pe_R	Péclet number based on the relative velocity (-)
R	capillary channel radius (m)
Re	Reynolds number (-)
r	radial distance (m)
r_0	radial position of vortex center (m)
r_1	radial position of dividing streamline (m)
S	surface area (m^2)
Sc	Schmidt number (-)
Sh	Sherwood number (-)
t, τ	time (s)
$\mathbf{u}, \mathbf{u}, \mathbf{w}$	velocity (radial and axial components) (m/s)
V	volume (m^3)
We	Weber number (-)
W	relative slip velocity (-)
x	coordinate (m)
Δx	mesh spacing (m)
z	axial distance (m)

Greek

δ	average thickness (film or boundary layer) (m)
θ	angle (rad)
κ	interface curvature
μ	dynamic viscosity (Pa.s)
σ	surface tension (N/m)
ρ	density (kg/m^3)
ϕ	level set distance function (m)
ξ	coordinate (m)

Subscripts

b	bubble
bs	bubble surface in contact with the slug
bf	bubble surface in contact with the film
cir	circulation
$diff$	diffusion
ds	dividing streamline
$film$	film
$film, b$	lubrication film in contact with the bubble (in between the two side stagnation points)
g	gas phase
gs	superficial gas phase
m	mass boundary layer
min	minimal
max	maximal
n	first normal derivative
nn	second normal derivative

l	liquid phase
loc	local
ls	superficial liquid phase
$pred$	predicted
s	slug
$slug\ core$	slug core region
t	tangential
tp	two-phase
uc	unit cell
Γ	interface
∞	steady state
Superscripts	
Gh	ghost values

in varying only one parameter at the time. Some of these correlations combine different contributions both from the film zone and the bubble caps, as proposed by Irandoust et al. [3] and van Baten and Krishna [9]. More sophisticated models are based on local characteristics of the flow or transfer fluxes, like the one suggested by Abiev [10, 11] which relies on a decomposition of the flow into three layers, but such models still require more local data to be validated and relevant scaling laws for the local mass transfer fluxes. In the experimental study of Butler et al. [1], local contributions of the film all along the channel wall and for the rest of the slug have been distinguished for the mass transfer process, showing some of the mechanisms involved: the whole transfer dynamic is strongly influenced by the recirculation motion in the slug, and the film surrounding the slug core contributes by feeding the rest of the slug in addition to the bubble caps, as it is a region rapidly enriched in dissolved gas. Such a contribution has been included in the theoretical framework proposed by Nirmal et al. [12]: the authors divide the system into different regions, the bulk slug, the liquid film surrounding the bubble and the liquid film close to the bulk slug, and solve (i) convection-diffusion equations for the concentrations in the liquid film in contact with the bubble and the surrounding bulk slug, and (ii) a modified version of such an equation in a coordinate system based on the streamsurfaces in the bulk slug, where the outermost streamline receives concentration both from the bubble caps and the surrounding liquid film. This modelling approach has shown potential for the prediction of the shrinkage rate of a dissolving bubble, but it still requires the knowledge of the relevant local transfer coefficients which are used as input in such a model or validations of their underlying assumptions. This can be achieved either through local experimental studies or Direct Numerical Simulations.

Experimentally, several issues make this task challenging. Indeed, it can be difficult to target a given cross-section of the flow [13], and therefore measure the gradients along the bubble interface. Then, local measurements are generally limited to a short time period. The latter issue can be solved by using a colorimetric technique to follow the solute absorption over a longer time [14], but such a method involves chemical reactions for which the kinetics need to be sufficiently slow compared to diffusion in order to avoid any acceleration of the intrinsic mass transfer rate. Finally, controlled conditions can be difficult to achieve in experiments, i.e. without surfactant effects or without an influence of the injection conditions of the two phases on the hydrodynamics and mass transfer characteristics. For example, in the investigation of Butler et al. [1] with the PLIF-I technique, some particular hydrodynamic features in the generated Taylor flow with a T-junction have been observed, showing the presence of zones richer in oxygen in the middle of the slugs for the cases of bubble Reynolds

number greater than 300, which could lead to some difficulties in the interpretation of the mass transfer rate.

Numerical studies offer a complementary approach, making it possible to work in ideal conditions and allowing for the computation of local fluxes along the interfaces. Several CFD simulations of Taylor flows have been carried out, including heat or mass transfer between the two phases or with the channel wall [9,15,16]. In order to be valid, these numerical simulations require the use of a mesh fine enough close to the wall so as to capture the thin lubrication film [16–19]. Moreover, the mesh also needs to be fine enough close to the interface so as to accurately resolve the transfer boundary layers. Because of these constraints, simulations at application-related values of the Schmidt number around bubbles of complex shapes have a very high computational cost, hardly affordable by Direct Numerical Simulations, especially at high Péclet number where a full grid independence of the results is difficult to achieve. Additionally, several works have used idealised shapes for the Taylor bubbles [9,20,21]. However, the exact shape of the bubble can produce interface regions with locally higher or lower rates of transfer [1,22]. Then, it is of interest to assess the transfer around Taylor bubbles of realistic shapes, a possibility being to use numerical methods able to compute the hydrodynamics around deformable bubbles and to maintain sufficient accuracy for interfacial mass transfer. Among recent works, such numerical methods simulate the hydrodynamics of Taylor bubbles by using the Volume of Fluid method [16,22–24], the Level-Set method [25,26], the Lattice Boltzmann method [27] or an interface tracking approach taking into account the bubble dissolution due to mass transfer [28]. A comparison of several computational results on the hydrodynamics with experimental data can be found in Marschall et al. [29]. Such a validation step based on experimental data or available theoretical results is of particular importance in order to ensure the accuracy of the numerical solution; indeed, Abadie et al. [26] have shown the existence of artificial additional recirculation loops when solving the hydrodynamics around a single Taylor bubble at small capillary number due to numerical spurious currents. Concerning the mass transfer dynamics, a full direct comparison between numerical simulations and local experimental results remains very challenging and has not yet been performed.

This work is a first step in the comparison of numerical and experimental results on the mass transfer dynamics in a train of Taylor bubbles. Simulations of trains of Taylor bubbles in the inertial regime (bubble Reynolds number higher than 100) are carried out: they correspond to four cases from the experimental study of Butler et al. [1], where the bubble shapes have been observed to be axisymmetric in the latter, and an additional case from the numerical work of Gupta et al. [18], also corresponding to axisymmetric conditions. The in-house DIVA code [30,31] for DNS, based on the Level-Set and Ghost Fluid methods, is employed to solve these Taylor flows. First, the hydrodynamics in a periodic unit cell is computed until steady-state, and bubble shapes and velocities are compared to experimental measurements or theoretical results. Then, mass transfer from the gas to the liquid is solved on the steady hydrodynamics (case of physical absorption), at low to moderate Schmidt numbers ($0.1 \leq Sc \leq 14$), by neglecting the bubble size decrease in time. The objective of this paper is to provide new insight on the mechanisms of mass transfer in a train of Taylor bubbles. The results will lead to the analysis of local Sherwood numbers for mass transfer fluxes both in the part of the interface in contact with the lubrication film and around the caps, allowing comparisons with previous simplified models when they are available. Finally, the global Sherwood number will also be scaled as a function of relevant non-dimensional numbers in this problem, allowing comparisons to the values obtained in our previous experimental study [1] at higher Schmidt numbers.

2. Numerical procedure

2.1. Governing equations

The two-phase flow is computed by solving the incompressible Navier-Stokes equations, which are written in the framework of a Eulerian one-fluid approach as:

$$\frac{\partial \mathbf{u}}{\partial t} + (\mathbf{u} \cdot \nabla) \mathbf{u} - \frac{\nabla \cdot (2\mu \mathbf{D})}{\rho} - \frac{\nabla P}{\rho} + \mathbf{g}, \quad \nabla \cdot \mathbf{u} = 0 \quad (1)$$

where \mathbf{u} is the velocity, P the pressure, ρ and μ the local values of density and dynamic viscosity respectively, \mathbf{g} the acceleration due to gravity and \mathbf{D} the rate of deformation tensor. Several of these variables are discontinuous across the interface, such as ρ , μ and P . By denoting $[P]_{\Gamma} = P_g - P_l$ the pressure jump at the interface, the balance of normal stresses at the interface leads to

$$[P]_{\Gamma} = \sigma \kappa + 2 \left[\mu \frac{\partial u_n}{\partial n} \right]_{\Gamma}, \quad (2)$$

where u_n is the velocity normal to the interface, \mathbf{n} the normal vector, σ the surface tension and κ the interface curvature. In the absence of surfactants or impurities adsorbed at the interface in this numerical study, the tangential stresses are assumed to be continuous across the interface.

Mass transfer is simulated by solving the advection-diffusion equation in the liquid phase, written on the mass concentration C of solute as:

$$\frac{\partial C}{\partial t} + (\mathbf{u} \cdot \nabla) C = D \Delta C, \quad (3)$$

with D being the diffusion coefficient associated with the considered binary fluid system.

2.2. Numerical methods

In this study, axisymmetric direct numerical simulations are carried out in the frame of the bubble, on Cartesian non-uniform meshes in order to accurately calculate both the bubble shape in equilibrium with the flow and the concentration gradients around the bubble, following the numerical procedure detailed in Lalanne et al. [30] concerning the hydrodynamics. It is briefly summarised here.

The governing equations are discretised by using by the finite volume method. For all equations, spatial derivatives in the diffusive terms are estimated with a second order central scheme and all the convective terms with a fifth order WENO scheme. Temporal derivatives are approximated with a second-order Runge-Kutta scheme. The capture of the interface on the mesh is ensured by the Level-Set method: the interface corresponds to the zero-level curve of a distance function ϕ , which is defined as the algebraic distance of each mesh point \mathbf{x} to the interface. Its displacement in the velocity field \mathbf{u} is tracked by solving the following equation for ϕ :

$$\frac{\partial \phi}{\partial t} + \mathbf{u} \cdot \nabla \phi = 0 \quad (4)$$

Additionally, an algorithm of redistancing is employed in order to ensure that ϕ remains a distance function at each time step, which consists of solving the following equation until steady state for a fictitious time τ :

$$\frac{\partial d}{\partial \tau} = \text{sign}(\phi)(1 - |\nabla d|) \quad (5)$$

where $d(\mathbf{x}, t, \tau)_{\tau=0} = \phi(\mathbf{x}, t)$. The Navier-Stokes equations (eq. 1) are computed by means of a projection method, with the jump condition (eq. 2) taken into account thanks to the Ghost Fluid Method.

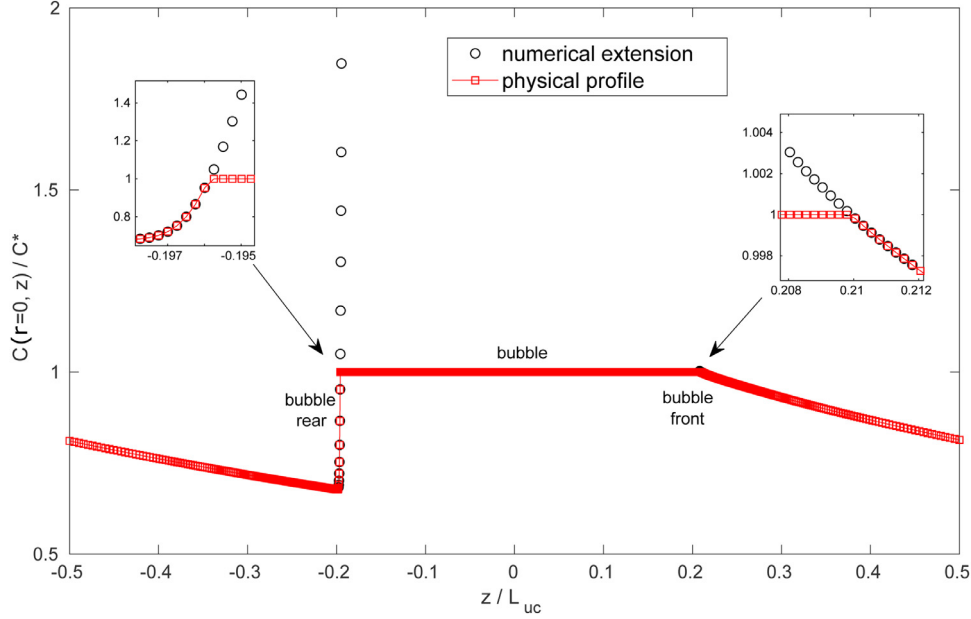


Fig. 1. Simulation B from Table 1 for $Sc = 10$, at $t = t_{cir}$ (defined later): concentration profile along the axis (red squares) and the extrapolated values inside the bubble close to the interface (black points). (For interpretation of the references to colour in this figure legend, the reader is referred to the web version of this article.)

For the mass transfer resolution, eq. 3 is computed with an explicit discretisation of the convective term and an implicit treatment of the diffusive term. Concentration is solved in the liquid phase only, with a Dirichlet boundary condition $C = C^*$ imposed on the immersed interface. To such a purpose, the method proposed by Gibou et al. [32] is used, which takes into account the Dirichlet condition during the discretisation of the Laplacian of the concentration in the cells close to the interface. Indeed, discretization of $\Delta C = f$ is written as $\frac{C_{i+1} - C_i}{\Delta x^2} + \frac{C_i - C_{i-1}}{\Delta x^2} = f_i$ at a grid node i in a one dimensional mesh of spacing Δx . If the immersed interface lies between the node $i - 1$, inside the bubble, and i , in the liquid, this discretization can no longer be written in that form as gradients are not computed in the gas; then, the method proposes to replace C_{i-1} by a fictitious value C_{i-1}^{Gh} calculated from a linear extrapolation between points $i - 1$ and i , which involves both the value C_i and the value C^* at the interface:

$$C^* = \theta C_{i-1}^{Gh} + (1 - \theta)C_i, \quad (6)$$

where θ is a distance ratio which indicates the position of the interface between the nodes $i - 1$ and i by $\theta = |\phi_i| / (|\phi_{i-1}| + |\phi_i|)$. Additionally, in order to maintain a high accuracy of the discretization of the convective term in eq. 3, a WENO scheme of 5th order is employed. Around the interface, such a discretization requires fictitious values of the concentration in the gas. These ghost values are generated by the second-order extension method introduced by Aslam [33]. It consists of solving three partial differential equations until steady state (on a fictitious time) at each time step, in order to preserve the continuity of the extrapolated function along the normal direction to the interface, by eq. 7 c, as well as the continuity of the first and second directional derivatives, by eq. 7 b and 7 a respectively:

$$\frac{\partial C_{nn}}{\partial \tau} + H(\phi) \mathbf{n} \cdot \nabla C_{nn} = 0 \quad (7a)$$

$$\frac{\partial C_n}{\partial \tau} + H(\phi) (\mathbf{n} \cdot \nabla C_n - C_{nn}) = 0 \quad (7b)$$

$$\frac{\partial C}{\partial \tau} + H(\phi) (\mathbf{n} \cdot \nabla C - C_n) = 0, \quad (7c)$$

where C_n and C_{nn} are respectively the normal first derivative and the normal second derivative of C , and $H(\phi)$ the Heaviside function centered on the interface position. An example of second-order fictitious values extrapolated in the gas phase from computed values in the liquid phase is given in Fig. 1 for a case of simulation of mass transfer around a Taylor bubble.

Computation of hydrodynamics with these numerical methods has been extensively validated in Lalanne et al. [30] for the case of rising and shape-oscillating bubbles and droplets at Reynolds numbers of order 100. Concerning the mass transfer computation and the related specific numerical treatments previously mentioned, they have already been used in benchmark two-phase flow configurations involving phase change like boiling, drop evaporation or condensation [31,34–37]. In Appendix A, new validations are provided in the case of mass transfer around a spherical bubble, (i) in a pure diffusive case and (ii) in case of a rising spherical bubble at Reynolds number close to 20 for different Schmidt numbers Sc . This procedure validates the ability of such a numerical simulation to compute the mass transfer flux at high Sc by using mesh grids which are not boundary-fitted, provided that the mass boundary layers are captured on several grid points.

2.3. Simulation of Taylor bubble cases

Axisymmetric trains of Taylor bubbles in a liquid flow are considered in this study. They correspond to four cases A-D of the experimental study of Butler et al. [1] in a vertical capillary tube of diameter $d = 3$ mm, which are either ascending (B-D) or descending flows (A). For each case, only one unit cell is modelled (one bubble surrounded by two half slugs, see Fig. 2), with periodic boundary conditions for the lower and upper domain boundaries. The bubble volume V_b , the bubble velocity u_b , and the unit cell length L_{uc} are taken from the set of experiments and used as inputs in the simulations, corresponding then to realistic Taylor bubble flows obtained in a T-junction experimental device. A fifth ascending case E of Taylor flow is considered, where the characteristics are directly taken from the numerical study of Gupta et al. [18], which allows for the simulation in a different tube diameter $d = 0.5$ mm, using the same approach. Table 1 displays the physical parameters related to these simulation cases, and Table 2 the corre-

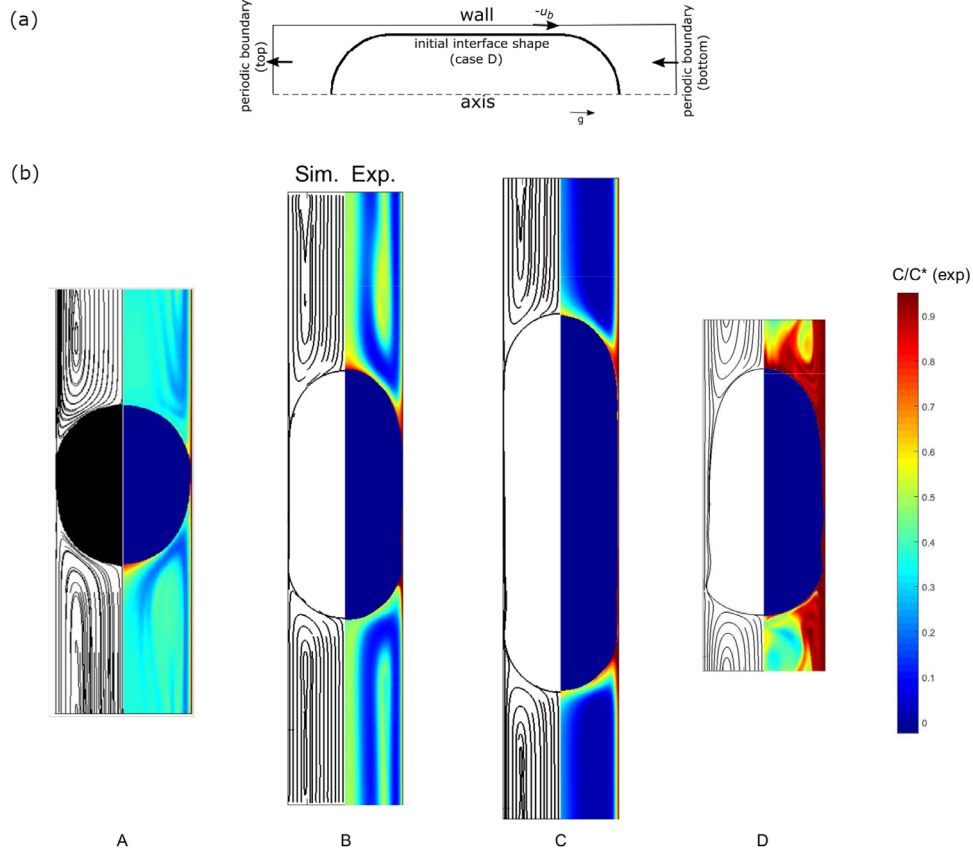


Fig. 2. (a) Initial and boundary conditions for the simulation of the hydrodynamics (case D), and (b) comparison between experimental and numerical final bubble shapes, with streamlines from the simulation (left) and concentration patterns of dissolved oxygen (right) from the experiments (see Butler et al. [1] for details on the experimental procedure). Cases A (descending flow), and B, C and D (ascending flows).

Table 1

Taylor flow input parameters for the five cases investigated for the hydrodynamical study, $g = -9.81 \text{ m/s}^2$ for cases B-E (ascending), $g = 9.81 \text{ m/s}^2$ for case A (descending). Cases A, B, C, D correspond respectively to cases labeled 10, 3, 2, 12 in Table 2 from Butler et al. [1]. Case E corresponds to the case simulated by Gupta et al. [18]. V_b is the bubble volume (given with accuracy as it is an input for the simulation), L_{uc} is the unit cell length, and d is the channel diameter.

Case	ρ_l (kg/m ³)	μ_l (mPa.s)	ρ_g (kg/m ³)	μ_g (mPa.s)	σ (mN/m)	d (mm)	V_b (m ³)	L_{uc} (mm)	u_b (m/s)
A	998	1.04	1.354	1.914×10^{-2}	72.8	3	1.73494×10^{-8}	10.2	-0.24
B	998	1.04	1.354	1.914×10^{-2}	72.8	3	3.63304×10^{-8}	15.8	0.1402
C	998	1.04	1.354	1.914×10^{-2}	72.8	3	5.75659×10^{-8}	17.0	0.094
D	1,006	4.20	1.354	1.914×10^{-2}	52.2	3	2.70839×10^{-8}	8.7	0.373
E	997	0.89	1.185	1.83×10^{-2}	72.0	0.5	1.47407×10^{-10}	1.65	0.55

Table 2

Dimensionless Taylor flow parameters for hydrodynamics and mass transfer for the five simulated cases. The mesh used to obtain an accurate resolution in the range of Pe considered is given. Note that the mesh is Cartesian and non-uniform, having smaller cells around the bubble than far from it in the z -direction, and keeping a uniform cell size Δx around the interface (same value in both the r and z -directions). In the lubrication film, in the r -direction, the mesh size is always equal to Δx for these grids except for the case A with the grid 457×1340 for which $\Delta x_{film} = 2.5 \mu\text{m}$. $Re_b = \frac{\rho_l |u_b| d}{\mu_l}$, $Ca = \frac{\mu_l |u_b|}{\sigma}$, $We = \frac{\rho_l u_b^2 d}{\sigma}$, $Pe = \frac{u_b d}{\nu_{cr}} = \frac{(|u_b| - 1/2 |u_b|) d^2}{L_d D}$.

Case	Re_b	Ca	We	$\frac{V_b}{V_{uc}}$	Pe range	mesh
A	691	3.4×10^{-3}	2.4	0.24	$17 \leq Pe \leq 838$	$457 \times 1,340$, or $670 \times 1,850$ for $Pe \geq 350$ $\Delta x = 3.3 \mu\text{m}$, or $\Delta x = 2.2 \mu\text{m}$ for $Pe \geq 350$
B	404	2.0×10^{-3}	0.8	0.33	$17 \leq Pe \leq 872$	$400 \times 2,100$, or $600 \times 3,150$ for $Pe \geq 650$ $\Delta x = 3.8 \mu\text{m}$, or $\Delta x = 2.5 \mu\text{m}$ for $Pe \geq 650$
C	271	1.3×10^{-3}	0.4	0.48	$18 \leq Pe \leq 272$	$220 \times 2,500$ $\Delta x = 6.8 \mu\text{m}$
D	268	3.0×10^{-2}	8.0	0.44	$11 \leq Pe \leq 142$	$380 \times 2,220$ $\Delta x = 4.0 \mu\text{m}$
E	308	6.8×10^{-3}	2.1	0.45	$25 \leq Pe \leq 308$	$160 \times 1,056$ $\Delta x = 1.6 \mu\text{m}$

sponding dimensionless numbers. The simulations are carried out in the frame moving with the bubble, with a wall velocity equal to $-|u_b|$.

Firstly, the hydrodynamics in the unit cell are simulated, by starting with an idealised bubble shape (two hemispheres and a cylindrical central body) of volume V_b as sketched in Fig. 2(a). A Poiseuille velocity profile is injected at the bottom of the domain, with an average value $u_{tp} - u_b$ in the frame of the bubble, where $u_{tp} = u_{gs} + u_{ls}$ is the average two-phase flow velocity and u_{gs} and u_{ls} are the superficial velocities of the gas and liquid phases respectively. On the top of the domain, the periodicity imposes continuity of axial velocity and its derivative in the axial direction. The simulation of the hydrodynamics is performed in order to find the equilibrium conditions in terms of bubble shape and velocity: the bubble must not translate in its frame of reference when the suitable u_{tp} value is imposed at the inlet. Starting from the experimental u_{tp} value, the bubble deforms and its velocity may change; then, the u_{tp} boundary value is adjusted. In the simulation, the choice has been made to update u_{tp} instead of the value of u_b because the experimental precision on the latter was higher [1]. The final value of u_{tp} , predicted by the simulation as the equilibrium velocity at a given u_b , is then compared to the expected value, as well as the final bubble shape and several geometrical properties of the bubble train (slug length, lubrication film thickness) from the experiments and simulations of Gupta et al. [18]. These comparisons are described below.

After convergence of the hydrodynamics, mass transfer from the gas to the liquid phase is computed in the periodic unit cell (physical absorption), starting with an initial solute concentration of zero in the liquid phase, and by using a Dirichlet condition at the interface ($C = C^*$ which is the saturation concentration of gas solute in the liquid phase at equilibrium), as well as a Neumann condition of vanishing flux at the wall, and periodic conditions at the upper and lower boundaries of the unit cell which ensure continuity of both the concentration and the flux in the axial direction. Simulations are performed for different Péclet numbers by varying the diffusion coefficient. The mass transfer dynamics is analysed in the corresponding section, with a focus on the concentration fields and the local mass transfer fluxes, before characterising the global Sherwood number.

For each simulation case, several Cartesian non-uniform mesh grids are employed, the final grids being presented in the Table 2. They are more refined in the bubble region, in order to accurately capture the concentration gradients around the interface, where the cells are uniform with a characteristic cell size Δx given for each case. Mesh convergence tests, which are introduced in each results section, have been performed to verify that both the hydrodynamics and mass transfer rate are accurately solved, knowing that the latter is more demanding at large Péclet number. In particular, the choice of these mesh grids for mass transfer, depending on the Schmidt number to be simulated, has been based on several sensitivity tests. The highest Péclet number for which the simulations of the different cases remain sufficiently precise on the mesh grids of Table 2 is limited by the computational resources available for this study.

3. Validation of hydrodynamics features

The hydrodynamics of the five simulation cases is only briefly described here as such Taylor flows are well-documented in literature. In all these cases, the normalised relative slip velocity $W = \frac{|u_b| - |u_{tp}|}{|u_b|}$ is lower than 0.5. Then, in agreement with the pioneering work of Taylor [38], the hydrodynamics involves circulation flows, as shown by the streamlines in the liquid slug in Fig. 2(b) for cases A-D. At the bubble interface, there are two stagnation points at the

symmetry axis and two further stagnation points on the side of the bubble - see also Fig. 3 where the stagnation points are marked by circles. A dividing streamline joins the side stagnation points of two adjacent bubbles in the train, therefore separating the circulation vortex from the liquid film along the wall. Based on the assumption that the slug is long enough to be described by a fully developed Poiseuille flow, Thulasidas et al. [39] gives the radial position $r_1 = R\sqrt{2 - \frac{|u_b|}{|u_{tp}|}}$ of the dividing streamline and the radial position $r_0 = \frac{R}{\sqrt{2}}\sqrt{2 - \frac{|u_b|}{|u_{tp}|}}$ of the vortex center where velocity is zero in the slug, as illustrated on Fig. 3 (where R is the capillary radius).

The following sections discuss the hydrodynamics against experimental and theoretical results for the five cases.

3.1. Bubble shape and film thickness

For the cases A-D, Fig. 2(b) presents a comparison of the numerical bubble shape in the unit cell, after the hydrodynamics is converged, with the experimental shapes from the study of Butler et al. [1]. In this figure, the computed streamlines from the simulation are displayed beside the concentration fields measured with the PLIF-I technique. Good agreement is obtained, both for the bubble shapes and patterns of the visible vortex with both approaches. Some spatial waves of the bubble shape in the film region are also clearly reproduced by the simulation, even though their position is slightly shifted in the case D. Such a good global matching confirms the suitability of the axisymmetric assumption for the computations of these experimental cases.

For some output parameters of the simulations (u_{tp} , lubrication film thickness δ_{film} , bubble length L_b), Table 3 compares the numerical values with the experimental ones (cases A-D) or with results from another simulation (case E), taken as reference. It can be seen that all these parameters are generally in very good agreement.

The values of the two-phase superficial velocities are very close to the values from these previous studies, with a maximal relative discrepancy of 7%. Concerning the geometry of the Taylor bubble, the bubble length is found to be similar to the references, with the maximal relative difference being only 4%. Concerning the film thickness, it is noted that it has been evaluated either by the minimal or average thickness of the nearly flat zone of the bubble (when such a flat zone exists, i.e for all cases except case A). The values are also very close to the reference values: results for cases A and D match very well with the experimental data, results for cases B and D show a discrepancy below 9%, there is only a higher difference on the film thickness value for the case C but which lies under the experimental uncertainty of $11\mu\text{m}$ [1.8], noting that similar values are found with simulations on different grids (76×680 and 220×2500) for this case C. As previously reported by Butler et al. [1], and confirmed by Table 3, δ_{film} can be satisfyingly predicted by the visco-capillary correlation of Aussillous and Quéré [40], valid for $Ca < 1$, under a precision of about 20% even if these inertial cases. The accuracy is similar with the correlation of Han and Shikazono [41], which takes into account an inertial contribution and which, in these five cases, only slightly increases the visco-capillary prediction by a maximum of 10%.

For case B, Table 4 shows the convergence of the results as a function of the number of mesh points in the lubrication film employed for three different tests. It can be seen that both the average liquid velocity u_{tp} and the film thickness are independent of the mesh using the two last grids, for which more than 10 grid cells are used to capture the lubrication film for this case. These last two grids were used for further mass transfer study.

From these detailed comparisons with experimental or other numerical or theoretical results, the simulations of hydrodynam-

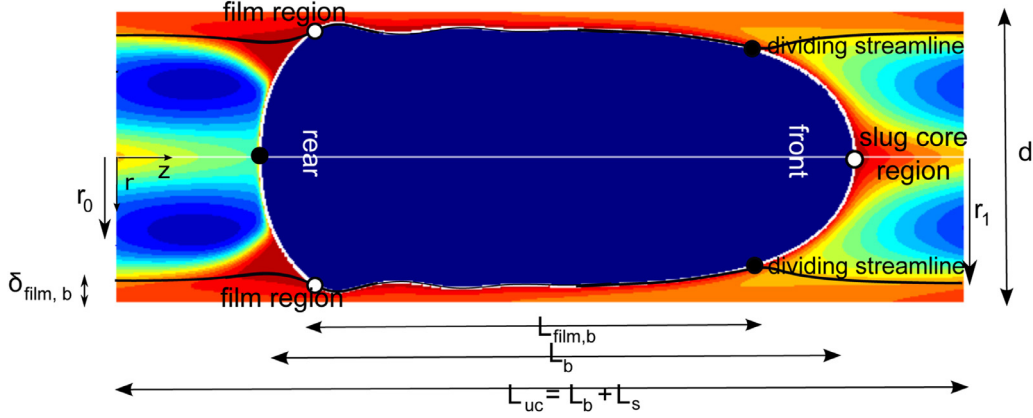


Fig. 3. Definition of parameters of the Taylor flow based on the hydrodynamics in the unit cell (Note the definition of the slug length $L_s = L_{uc} - L_b$). $\delta_{film,b}$ is defined as the average value in the film region between the two stagnation points on the side of the bubble; it is nearly equal to the average lubrication film thickness δ_{film} computed in the zone of nearly flat interface. Division of the whole slug into two regions for mass transfer analysis: the “film” and the “slug core” regions. Simulation case D at $Pe = 214$.

Table 3

Simulation results (“sim.”) of u_{tp} , minimal lubrication film thickness δ_{min} , average lubrication film thickness δ_{film} (in the nearly flat zone) and normalised bubble length L_b/d , compared to previous works (“ref.”): experimental values for cases A-D [1,8] where the experimental uncertainty corresponds to ± 1 pixel size, which was approx. $11\mu\text{m}$ close to the film region, and numerical values for case E [18]. Comparison to prediction values (“pred.”) according to the correlations of Aussillous and Quéré [40] and Han and Shikazono [41].

Case	δ_{min} (μm)		δ_{film} (μm) - Average value in the flat zone				u_{tp} (m/s)		L_b/d	
	sim.	ref.[1],[18]	sim.	ref.[1],[18]	pred.[40]	pred.[41]	sim.	ref.[1],[18]	sim.	ref.[1],[18]
A	24.6	23.6	No flat zone		42.4	46.1	-0.229	-0.217	1.21	1.27
B	24.0	29.3	38.6	42.3	30.3	31.7	0.133	0.124	2.12	2.17
C	20.9	18.7	30.1	23.0	23.5	24.2	0.086	0.086	3.26	3.30
D	114.9	118.1	176.7	182.5	146.7	151.4	0.292	0.275	2.05	2.05
E	7.8	-	11.1	12.0	10.7	11.3	0.503	0.500	2.00	2.00

Table 4

Mesh convergence of hydrodynamics calculation for case B. N_{film} is the number of grid cells in the lubrication film.

Mesh grid	u_{tp} (m/s)	Average film thickness δ_{film} (μm)
$256 \times 1,900$ $N_{film} = 6$	0.134	32.1
$400 \times 2,100$ $N_{film} = 10$	0.133	38.4
$600 \times 3,150$ $N_{film} = 15$	0.133	38.6

ics in the frame moving with the bubble can be considered to be validated, for the five cases.

3.2. Velocity profiles

For case B, Fig. 4 displays the numerical velocity profiles in the radial direction, both in the liquid phase only at the top of the domain, and at the middle of the bubble along a radial line including the gas phase and the film. In the plot, these profiles are compared with the theoretical solution obtained by Abiev [42] by solving the Navier-Stokes equations with continuity of both velocities and tangential stresses at the interface, under the assumption of a fully-established hydrodynamics, which leads to:

- in the liquid slug:

$$w(r) = 2u_{tp} \left[1 - \left(\frac{r}{R} \right)^2 \right] \quad (8)$$

- in the lubrication film, for $R - \delta_{film} \leq r \leq R$:

$$w(r) = E_1 (R^2 - r^2) - C_1 \ln \left(\frac{R}{r} \right) \quad (9)$$

$$\text{with } E_1 \text{ a constant and } C_1 = (\rho_l - \rho_g) g \frac{(R - \delta_{film})^2}{2\mu_1},$$

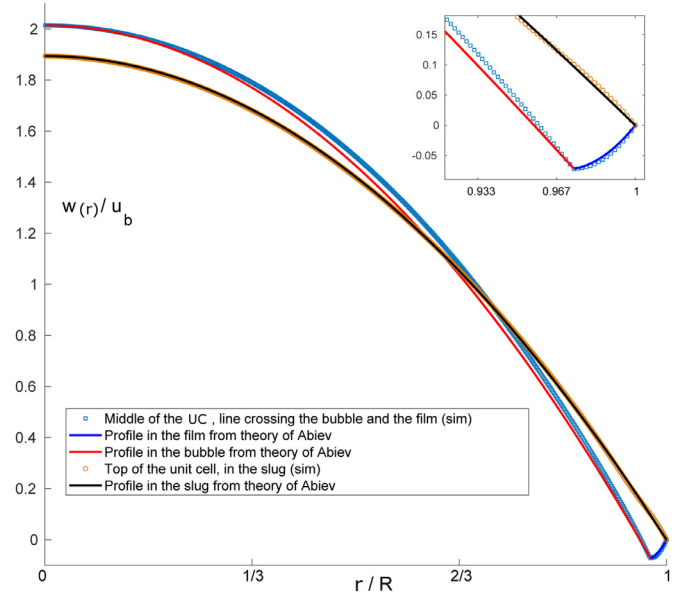


Fig. 4. Radial velocity profiles for simulation case B, in the frame of the laboratory, taken in the middle of the unit cell UC (upper boundary of the domain), and in the middle of the bubble which includes both the gas bubble and the lubrication film. Theoretical comparisons are based on the work of Abiev [42].

- inside the bubble, for $0 \leq r \leq R - \delta_{film}$:

$$w(r) = E_1 (R^2 - (R - \delta_{film})^2) + E_2 \left((R - \delta_{film})^2 - r^2 \right) - C_1 \ln \left(\frac{R}{R - \delta_{film}} \right) \quad (10)$$

with E_2 being another constant.

Note that, for the numerical computation of eq. 9 and 10, constants E_1 and E_2 have been evaluated so as to match the velocity value at the axis and at the bubble interface respectively. Profiles are observed to be in very good agreement between this analytical solution and the numerical results. The very slight discrepancy along the middle line is attributed to the fact that the velocity profile extracted at the middle of the bubble is close to but not fully independent of the axial coordinate, the assumption of established flow in the bubble and in the lubrication film being a good approximation. In the slug of liquid, the profile at the top is identical to that imposed at the bottom of the unit cell, the slug being long enough for the flow to be fully established.

4. Mass transfer analysis

In this section, the mass transfer dynamics is simulated based on the converged hydrodynamics previously described, under the assumptions that (i) the resistance to mass transfer is negligible in the gas phase compared to that in the liquid phase (which allows for the solving of the concentration fields in the liquid phase only, thus neglecting the concentration gradients inside the bubble and considering a Dirichlet boundary condition for the concentration at the interface based on the thermodynamics equilibrium between the liquid and the gas phases), (ii) the interface is at the saturation concentration C^* , as given by the thermodynamics, and (iii) the rate of mass transfer is considered to be low enough so the total volume of the bubble does not change in time and that the average concentration in the gas phase remains constant.

For cases A-E, simulations are performed at different Péclet numbers by varying the diffusion coefficient D . For these Taylor flows, we define a Péclet number to characterise mass transfer as $Pe = \frac{t_{diff}}{t_{cir}} = \frac{(|u_{tp}| - \frac{1}{2}|u_b|)d^2}{L_s D}$ by comparing the relative importance of a diffusion time scale d^2/D at a length scale d (close to the diameter of the bubble caps) and a convective time scale t_{cir} which characterises the recirculation time in the vortex of the slug of length L_s ($L_s \geq d$). For t_{cir} , the expression from Thulasidas et al. [39] is used:

$$t_{cir} = \frac{\pi L_s r_0^2}{2\pi \int_0^{r_0} 2|u_{tp}| \left(1 - \left(\frac{r}{r_0}\right)^2\right) - |u_b| \int_0^{r_0} r dr} = \frac{L_s}{|u_{tp}| - \frac{1}{2}|u_b|}, \quad (11)$$

based on the assumptions that the velocity profile in the slug is a Poiseuille flow and that the recirculation region is cylindrical, of length L_s and radius r_0 . Fig. 3 displays an example of concentration field obtained for the simulation case D, as well as the main geometric parameters which describe Taylor flow.

Pe is varied up to values of 900 (see Table 2). Its value is chosen (by varying the diffusivity in the simulations) so as to accurately simulate mass transfer by respecting the condition that several grid cells are present in the regions of the interface where the concentration gradients are the highest, which cannot be estimated before running the simulations contrary to the case of transfer around spherical rising bubble in an unconfined medium. Validation of mass transfer calculations was achieved by mesh convergence tests. Indeed, for case A, Fig. 7 presents the time evolution of the Sherwood number for two simulations at high Pe with different grid resolutions, showing that their discrepancy is lower than 3%. Then, for cases A-E, results on the Sherwood number in the steady regime computed on several grids are given in Appendix B, and are found to be almost identical when changing the mesh size, which justifies the range of Pe chosen for this study. It has been observed that, with this numerical method, the results are mesh-converged provided that the mass boundary layer, at its thinnest point, is described by at least 8 mesh cells.

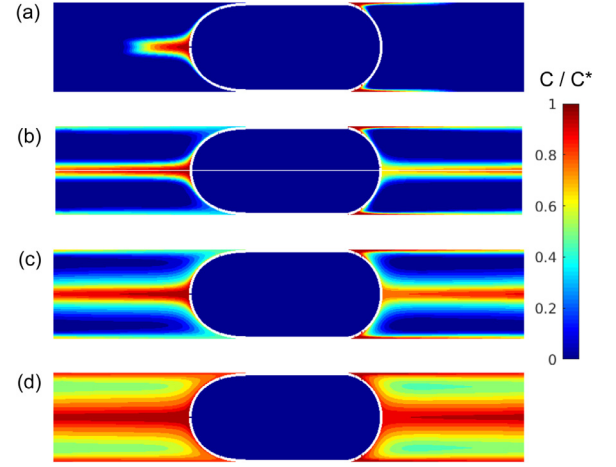


Fig. 5. Normalised concentration fields for simulation case B for $Sc = 10$, $Pe = 686$, at (a) $t = 0.2 t_{cir}$, (b) $t = 0.8 t_{cir} = 1.1 L_{uc}/|u_b|$, (c) $t = 2.1 t_{cir}$, (d) $t = 10.8 t_{cir}$. Note that the bubble concentration is artificially set to 0 in the figure.

4.1. Dynamics of mass transfer in Taylor flow

Fig. 5 shows the time evolution of the concentration field in the liquid, for case B for $Pe = 686$. At very short time, as diffusion begins, a mass transfer boundary layer appears around the interface. Then, as seen in Fig. 5 (a), two convective effects transport the solute (i.e. oxygen) in parallel. Firstly, along the central axis, oxygen travels from the bubble front towards the rear of the preceding bubble in the train because the liquid velocity is higher than that of the bubble along the symmetry axis. This process has a characteristic time of approximately $L_s/(2|u_{tp}| - |u_b|)$ based on the relative liquid velocity at the axis. Secondly, at the outlet of the lubrication film between the near-flat bubble interface and the wall, the relative velocity in the film, close to $|u_b|$, convects oxygen towards the following bubble for a time $t_{film} \approx L_{uc}/|u_b|$. Note the presence of a filament of dissolved oxygen nearly attached to the bubble rear, close to the convergent stagnation point (also visible in Figs. 9(b) and 11(b), where the convergent stagnation point is indicated with a white circle), which is slowly convected in the same direction as the flow in the film. The presence of this filament has also been reported in the experiments of Butler et al. [1] and the simulations of Silva et al. [22] with isolated Taylor bubbles (denoted as a concentration plume).

As soon as the solute is convected to the neighboring bubble in the train, the concentration fields in the different unit cells become interdependent (Fig. 5 (b)). In a given unit cell, the transfer process both from the bubble caps and the bubble film along the wall continues, and, in the slug core, diffusion occurs across the circulation motion (Fig. 5 (c)), leading to patterns of concentration that follow the streamlines (high Pe), with the vortex center being the point of lowest concentration in the unit cell.

In addition to solute transfer coming from the bubble interface, the slug core is also fed by an exchange flux originating from the liquid film along the wall, that surrounds the bulk slug, as it is a zone richer in oxygen. This process of mass exchange connects the different unit cells due to the film continuity and is analogous to the cross talk mechanism in the multizone model proposed by Nirmal et al. [12]. Here, it is found that the ratio of this exchange flux, i.e mass transfer from the liquid film into the core of the slug to the flux coming from the bubble caps, increases with Pe , and reaches values close to 1 for Pe of approximately 500. For values of Pe large enough that convection is faster than radial diffusion, the characteristic thickness of the liquid film surrounding the bulk

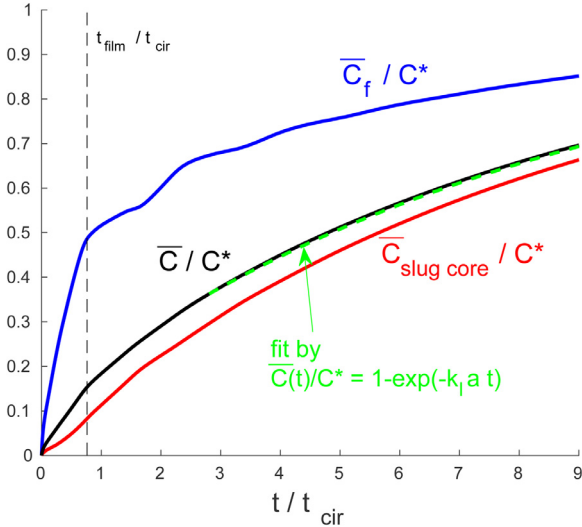


Fig. 6. Time evolution of the normalised average concentration $\bar{C}(t)/C^*$ in the liquid (and fitting by eq. 17), and for both the film and slug core region (as defined in fig. 3). Simulation case B for $Pe = 490$.

slug can be described by $R - r_1$, where r_1 is the radial position of the dividing streamline (see Fig. 3).

All these local transfer fluxes need their own times to fully establish, after which the unit cell concentration field remains qualitatively the same other than values that increase with time, like between Fig. 5(c) and (d). Based on these different characteristic zones of the mass transfer process, Fig. 3 proposes a separation of all the liquid into a "slug core" region (the bulk slug) and a "film" region, all along the wall, which includes by continuity both the lubrication film along the bubble and the liquid surrounding the slug core.

The transient mass transfer process can be characterised thanks to the time evolution of the average concentration $\bar{C}(t)$ in the liquid: from the local Eulerian field $C(r, z, t)$ in the simulation, the average concentration is computed as

$$\bar{C}(t) = \frac{1}{V_l} \iiint_V C dV, \quad (12)$$

where dV is the elementary volume element and $V_l = V_{uc} - V_b$ is the volume of liquid in the unit cell, with V_{uc} equal to the unit cell volume and V_b the bubble volume. The instantaneous total transfer flux J at the interface is also computed, from which the mass transfer coefficient k_l is determined:

$$J(t) = -D \nabla C \cdot \mathbf{n} dS = k_l(t) S_b (C^* - \bar{C}(t)) \quad (13)$$

(with S_b the bubble surface area), then it is included in the global Sherwood number:

$$Sh(t) = \frac{k_l(t) d}{D}. \quad (14)$$

Note that, from an unsteady mass balance of solute dissolved in the liquid, the Lagrangian time derivative of $\bar{C}(t)$ can be related to the total transfer flux $J(t)$ at the bubble surface by

$$V_l \frac{D\bar{C}(t)}{Dt} = \iint_b -D \nabla C \cdot \mathbf{n} dS + \iint_{uc \text{ boundaries}} \mathbf{j} \cdot \mathbf{n} dS = J(t), \quad (15)$$

with \mathbf{j} the diffusive flux. Indeed, the second integral in the right hand side of eq. 15 vanishes because the flux is null at the wall and at the symmetry axis, and the integral $\mathbf{j} \cdot \mathbf{n} dS$ on both the upper and lower unit cell boundaries is also null due to the periodicity condition.

Fig. 6 presents the time evolution of $\bar{C}(t)/C^*$ for case B for $Pe = 490$, and partial averages in the "film" and "slug core" regions

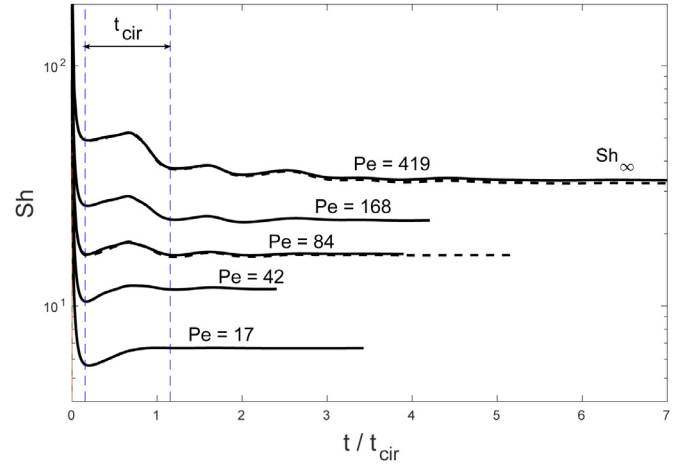


Fig. 7. Time evolution of the Sherwood number. The two dashed lines correspond to simulations carried out with a mesh with a lower number of grid cells to verify the mesh independence of the results ($457 \times 1,340$ vs. $670 \times 1,850$). Simulation case A.

computed by eq. 12 in these specific areas (defined in fig. 3). The concentration in the film is always much higher than that in the slug core region, and increases strongly at first until the convective time t_{film} is reached, before displaying a slower dynamic. In parallel, Fig. 7 displays the time evolution of the global Sherwood number Sh . It can be seen that its value is initially very large, before decreasing rapidly during the fast establishment of the mass boundary layers around the interface. This has also been seen in simulations of heat transfer around single Taylor bubbles performed by Zhang et al. [43]. Then Sh continues to slowly decrease by presenting damped oscillations at a higher frequency than its time decrease. These oscillations are controlled by the circulation motion in the slug since their period corresponds to the theoretical circulation time t_{cir} , as computed by eq. 11. This periodic renewal of fresh liquid close to the caps causes such variations of Sh . Such an oscillating behaviour is characteristic of a transfer process in a region of closed streamlines, such as mass or heat transfer inside a droplet [44]. This also confirms that t_{cir} is a relevant convective time scale of the problem.

Concerning the long-term evolution in fig. 7, the global Sh always reaches a plateau denoted Sh_∞ , and therefore an associated constant mass transfer coefficient $k_{l,\infty}$. The higher the Pe , the smaller the rate of damping of $Sh(t)$, leading to a larger time required to reach Sh_∞ . In this steady regime for Sh , the average concentration $\bar{C}(t)$ in the liquid continues to increase while the transfer flux decreases, leading to:

$$V_l \frac{D\bar{C}}{Dt} = k_{l,\infty} S_b (C^* - \bar{C}(t)) \quad (16)$$

whose solution is

$$\bar{C}(t)/C^* = 1 - \exp\left(-k_{l,\infty} \frac{S_b}{V_l} t\right) \quad (17)$$

with $k_{l,\infty} S_b / V_l = k_l a$ generally called the volumetric mass transfer coefficient. Such a fitting function can be verified in fig. 6. It is worth noting here that a unique $k_l a$ value for mass transfer in Taylor flow can be measured only in the case where the mass transfer process has reached steady state and such a fitting function should not be used from the beginning. The time required to reach the steady regime will be presented later in Section 4.4.

4.2. Local fluxes along the interface

The mass transfer dynamics previously described are similar for all the Taylor flows considered here. To analyse these com-

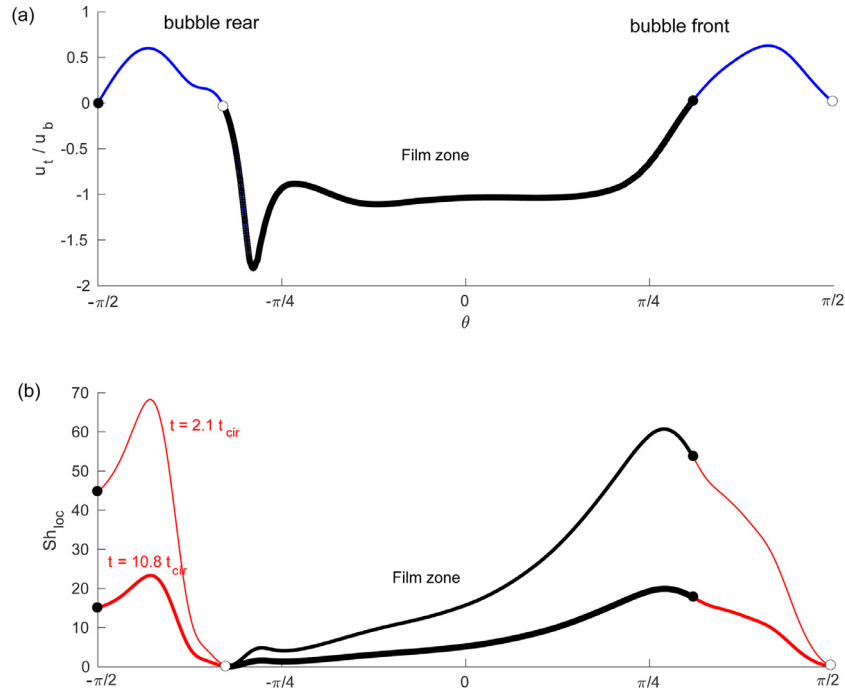


Fig. 8. Normalised tangential velocity $u_t/|u_b|$ (in the frame of the bubble) and local Sherwood number Sh_{loc} along the interface. Simulation case B at $Pe = 686$. The white points correspond to the locations of the convergent stagnation points (the tangential velocity around these points is directed towards them) and the black points to that of the divergent stagnation points (with tangential velocity escaping from these points).

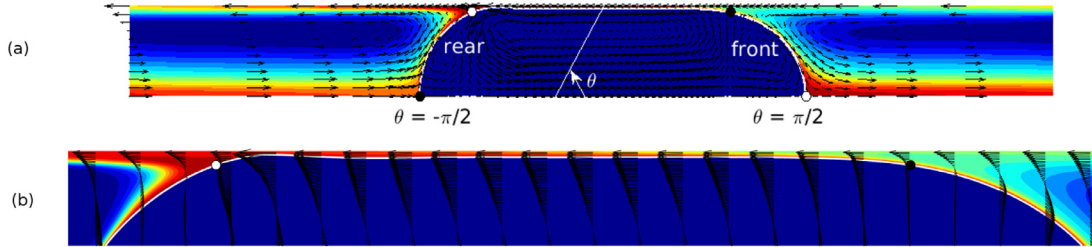


Fig. 9. Velocity and concentration fields in the liquid phase only. Simulation case B for (a) $Pe = 686$, at $t = 2.1 t_{cir}$ as in fig. 8, for (b) $Pe = 1,743$ at $t = 1.1 t_{cir}$ (this high Pe case is presented for illustration purposes only). White points: convergent stagnation points, black points: divergent stagnation points.

mon features, Figs. 8 and 10 present profiles of both the local Sherwood number $Sh_{loc} = -\frac{\mathbf{n} \cdot \nabla C}{C_*} d$ and the normalised tangential velocity $u_t/|u_b|$ in the frame of the bubble, along the bubble interface (along the θ polar angle), for cases B and A, respectively. The concentration and velocity fields for these cases are displayed in fig. 9(a) and 11(a) respectively. At the bubble surface, the four stagnation points (two convergent and two divergent points) are marked and are of particular interest to describe the mass flux distribution. For these Taylor bubbles of non-ideal shapes, the "film zone" of the interface can precisely be defined as the bubble surface between the two stagnation points which are close to the channel wall. Along this film zone, it is noted that the magnitude of tangential velocity is close to $|u_b|$ and presents a local maximum at the place where the film thickness is minimal. Two other local maximal values of the tangential velocity are also observed along the caps, which are each other of comparable magnitude (lower than $|u_b|$).

The spatial distribution of Sh_{loc} around the interface presents two locations of maximal values: (i) close to the divergent stagnation point at the entrance of the film, and (ii) at the bubble rear, at the point where the tangential velocity is maximal. As shown here with cases A and B, the importance of these two local maximum values is not systematically the same, despite their locations being similar. They correspond to the interface points where the

mass boundary layer is locally thinnest at all times because it is pressed against the bubble by the circulation flow within the slug. Moreover, even though the evolution of the tangential velocity is comparable between the front and the rear cap, note that their profiles of mass flux density are different. However, by considering the surface integral of the flux density along each cap separately, it can be seen that they both significantly contribute to the transfer towards the slug core region. It is worth noting that this behavior strongly differs from the case of external transfer around a freely rising bubble, for which the two hemispheres have very contrasted integral contributions with much higher fluxes on the northern hemisphere compared to the southern [45].

In the film region of the interface, based on figs. 9(b) and 11(b), starting from the black point where the flux is maximal and following the direction of the flow (from the bubble front to the rear), the interfacial flux decreases until being zero at the white convergent stagnation point (end of the film). This decrease can be linked to a growth of the mass boundary layer while the liquid film travels along the interface. At the end of the film, the vanishing flux can be related to the presence of a stagnant concentration plume visible on the concentration fields of figs. 9(b) and 11(b) around the white points.

These common features in terms of local transfer fluxes profiles around the interface of these Taylor bubbles, either in de-

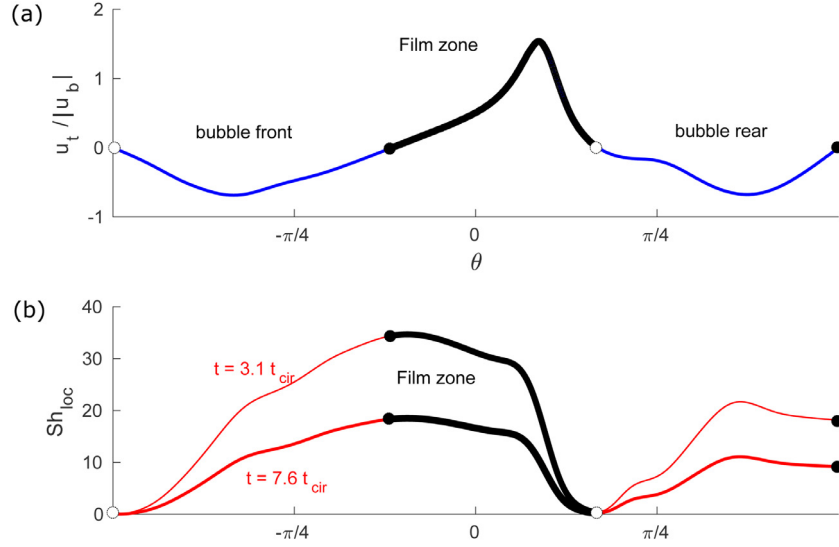


Fig. 10. Normalised tangential velocity $u_t/|u_b|$ (in the frame of the bubble) and local Sherwood number Sh_{loc} along the interface. Simulation case A at $Pe = 419$. White points: location of the convergent stagnation points, black points: location of the divergent stagnation points.

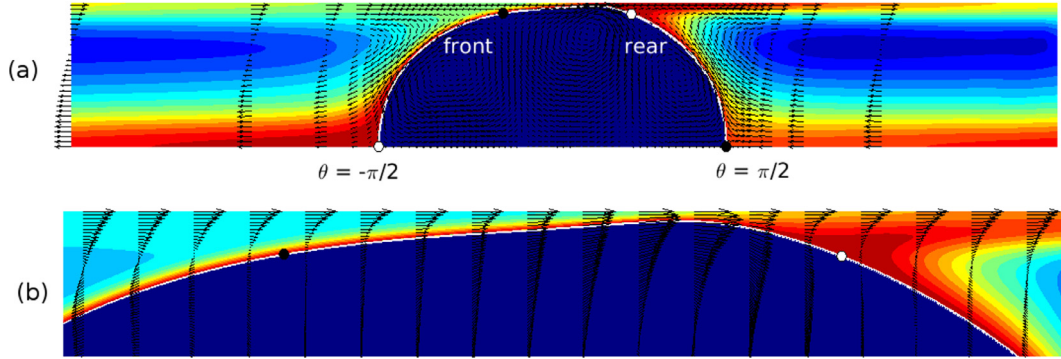


Fig. 11. Velocity and concentration fields in the liquid phase only. Simulation case A for (a) $Pe = 419$, at $t = 3.1t_{cir}$ as in fig. 10, for (b) $Pe = 1,197$ at $t = 1.8t_{cir}$ (this high Pe case is presented for illustration purposes only). The two white points correspond to the convergent stagnation points and two black points to the divergent stagnation points. White points: convergent stagnation points, black points: divergent stagnation points.

scending or ascending flows, suggest that a common correlation for the global Sherwood number can be proposed. Before analysing the global Sh_∞ in Section 4.4, local Sherwood numbers integrated per zone are discussed in the following sections.

4.3. Local Sherwood numbers

In this section, the local fluxes are quantified through local Sherwood numbers for transfer across the "film zone" of the interface, across the bubble caps (including both the front and rear cap), and the internal exchange flux between the film region along the wall and the slug core. The local Sherwood numbers are computed once they reach steady values.

4.3.1. Transfer across the film zone of the bubble interface

Transfer in the lubrication film is mainly driven by diffusion in the transverse direction and by convection in the axial direction. Even though the film is stagnant in the frame of the laboratory, its relative velocity with the bubble, of magnitude very close to $|u_b|$ based on the velocity profiles in the film (fig. 4), induces convective transfer. From the DNS results, the transfer flux across the film zone of the interface can be measured by integration along the corresponding surface S_{bf} , from which the local mass transfer

coefficient k_{bf} can be determined:

$$J_{bf}(t) = \int_{S_{bf}} -D \nabla C \cdot \mathbf{n} dS = k_{bf} S_{bf} (C^* - \bar{C}_f(t)). \quad (18)$$

The corresponding local Sherwood number Sh_{bf} is then computed from

$$Sh_{bf} = \frac{k_{bf} \delta_{film,b}}{D} \quad (19)$$

by considering an average uniform film thickness $\delta_{film,b}$ of length $L_{film,b}$ for the lubrication film along the bubble (note that $\delta_{film,b}$, defined between the two side stagnation points, is equal or 5% greater than the average thickness δ_{film} evaluated in the flat region of the interface for the cases B-E).

These values Sh_{bf} will be compared to the simplified model of mass transfer in the film surrounding the bubble, proposed by Irandoust et al. [3], Eskin and Mostowfi [46] and Nirmal et al. [12], which relies on assumptions that were not yet validated against direct measurements of the transfer flux in the film. This model considers only the dominant transfer mechanisms in the axial and radial directions, neglecting the velocity gradients in the lubrication film, and assuming that the film thickness is small compared to the channel radius. This model, at steady state, predicts a concentration profile $C_{film,pred}(x, z)$ in the film given by

$$|u_b| \frac{\partial C_{film,pred}}{\partial z} = D \frac{\partial^2 C_{film,pred}}{\partial x^2}, \quad (20)$$

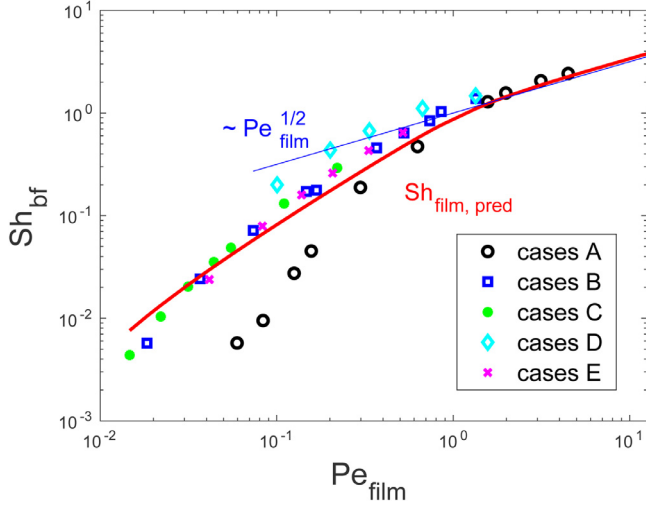


Fig. 12. For all cases, local Sherwood numbers in the film zone of the interface, Sh_{bf} , as a function of the film Péclet number $Pe_{film} = \frac{|u_b| \delta_{film,b}^2}{L_{film,b} D}$. Comparison with the prediction of the simplified analytical solution giving $Sh_{film,pred}$ from eq. 23.

by using a Cartesian coordinate system where $x = 0$ corresponds to the bubble interface and $x = \delta_{film,b}$ to the wall. The film is located in the range $0 \leq x \leq \delta_{film,b}$ and extends in the axial direction between $z = 0$ and $z = L_{film,b}$. For the specified model boundary conditions, $C_{film,pred}(x = 0, z) = C^*$, $C_{film,pred}(x, z = 0) = C_0$ and $\partial C_{film,pred} / \partial x (x = \delta_{film,b}, z) = 0$, the analytical solution of eq. 20 can be written as

$$\frac{C_{film,pred}(x, z) - C^*}{C_0 - C^*} = \frac{2}{\pi} \sum_{n=1}^{\infty} \frac{1 - (-1)^n}{n} \exp \left[- \left(\frac{\pi n}{2} \right)^2 \frac{Dz}{|u_b| \delta_{film,b}^2} \right] \sin \left(\frac{\pi n}{2} \frac{x}{\delta_{film,b}} \right) \quad (21)$$

Then, the local mass transfer coefficient predicted by this model can be computed from

$$k_{bf,loc,pred}(z) = \frac{-D \partial C_{film,pred} / \partial x (x = 0, z)}{C^* - C_0} \quad (22)$$

leading to a predicted Sherwood number for the film $Sh_{film,pred}$ given by

$$Sh_{film,pred} = \frac{\delta_{film,b} \frac{1}{L_{film,b}} \int_0^{L_{film,b}} k_{bf,loc,pred}(z) dz}{D} \quad (23)$$

Note that $Sh_{film,pred}$ is independent of the value of C_0 , therefore, for simplicity, it can be taken that $C_0 = 0$.

The film Péclet number is defined as $Pe_{film} = \frac{|u_b| \delta_{film,b}^2}{L_{film,b} D}$ which is the ratio of the diffusion time scale $\delta_{film,b}^2/D$ and the convection time scale $L_{film,b}/|u_b|$ in the film. In this model, the third boundary condition $\partial C_{film,pred} / \partial r (r = \delta_{film,b}, z) = 0$ is only valid provided that the mass boundary layer that develops in the film, with characteristic thickness $\delta_{m,bf}$, remains small compared to the average film thickness $\delta_{film,b}$. From eq. 20, which balances a convective flux of order $\frac{|u_b| C_{film,pred}}{L_{film,b}}$ to a diffusive flux of order $\frac{D C_{film,pred}}{\delta_{m,bf}^2}$, it can easily

be shown that $\frac{\delta_{m,bf}}{\delta_{film,b}} \sim \frac{1}{\sqrt{Pe_{film}}}$, proving that the prediction given by eq. 23 will only work for sufficiently large Pe_{film} . Under this condition, the film theory shows that the Sherwood number in the film is given by $Sh_{film,pred} \sim \frac{\delta_{film,b}}{\delta_{m,bf}}$, leading to $Sh_{film,pred} \sim \sqrt{Pe_{film}}$.

Fig. 12 plots the Sherwood number characterising mass transfer across the bubble film Sh_{bf} obtained from the DNS results as

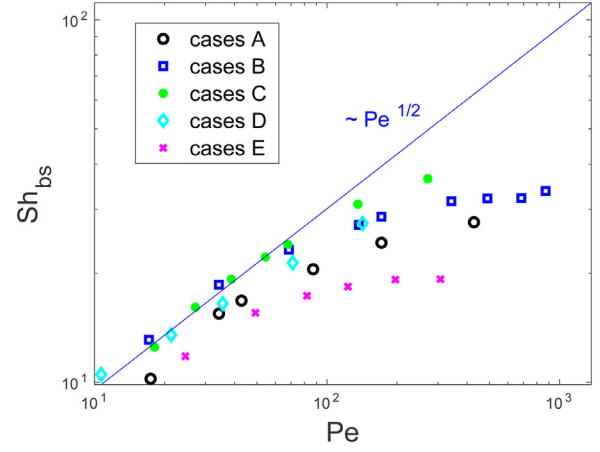


Fig. 13. For all cases, local Sherwood numbers in the bubble cap regions of the interface, Sh_{bs} , as a function of the Péclet number $Pe = \frac{(|u_b| - \frac{1}{2}|u_b|) d^2}{L_s D}$. A similar trend is obtained as a function of $Pe_b = \frac{|u_b| d}{D}$ instead of Pe .

a function of Pe_{film} . It compares the solution with the predicted value $Sh_{film,pred}$ computed from the simplified literature model presented above (eq. 23). From the results, it is clear that Pe_{film} is a relevant parameter to quantify the rate of transfer across the bubble film: numerical results of cases B, C and E lie on a single curve for any Pe_{film} ; those from cases A and D follow a different trend for $Pe_{film} \ll 1$ but tend towards the same curve as the other cases for Pe_{film} of order unity. Indeed, for the latter Taylor flow cases, the shape of the bubble is farthest from the case of a long flat film interface, possibly explaining the different behaviours at small Pe_{film} . Interestingly however, when $Pe_{film} \geq 0.7$, the figure shows that the scaling law $Sh_{bf} \sim \sqrt{Pe_{film}}$ accurately matches the DNS results of the mass flux in the film, for the cases A, B and D. Furthermore, for several points of case A at $Pe_{film} \geq 1$, the prediction $Sh_{film,pred}$ is very close to the numerical values Sh_{bf} . Such a result suggests that the simplified model with a 1D convection-diffusion equation is suitable for predicting the mass transfer coefficient in the film for $Pe_{film} > 1$, which is an important result, in practice, for further modelling.

4.3.2. Transfer across the two bubble caps

In this section, the transfer from the bubble caps to the slug core region is quantified. This corresponds to the surface areas between the stagnation points along the axis and those approaching the film zone. As such, $S_{bf} + S_{bs} = S_b$. From the DNS results, the transfer flux is integrated along the bubble caps surface, and from which the local mass transfer coefficient k_{bs} can be determined

$$J_{bs}(t) = \iint_{S_b} -D \nabla C \cdot \mathbf{n} dS = k_{bs} S_{bs} C^* - \bar{C}_{slug\ core}(t) \quad (24)$$

The corresponding local Sherwood number is computed from

$$Sh_{bs} = \frac{k_{bs} d}{D} \quad (25)$$

Fig. 13 plots the evolution of Sh_{bs} as a function of the Péclet number Pe , for all simulation cases. Note that the evolution as a function of $Pe_b = \frac{|u_b| d}{D}$ is very similar but Pe appears more suitable for describing the ratio between convective and diffusive processes in a unit cell with two distinct characteristic lengths. Results from the DNS show that there exists a dependence of $Sh_{bs} \sim \sqrt{Pe}$ at moderate Pe numbers up to approximately 100. However, for larger Pe , Sh_{bs} increases by a lower rate, tending even to saturate at large Pe at thresholds which appear to be case dependent. These saturation values may depend on both Re_b and the geometrical properties of the slug core region. Such an evolution can be related to

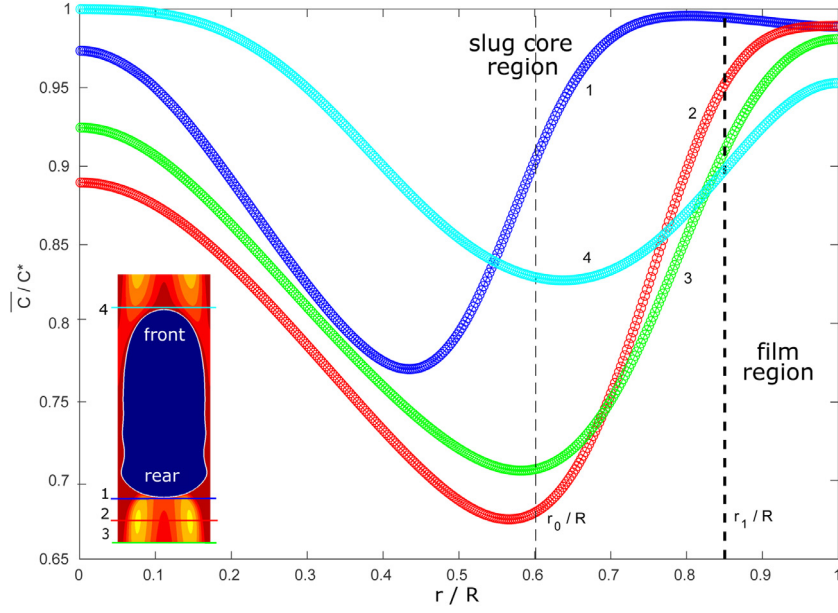


Fig. 14. Radial concentration profiles in the liquid slug at different z levels. Simulation case D for $Pe = 142$.

the fact that the slug core is a region of closed streamlines, exactly like the Hill vortex inside a moving droplet. Indeed, studies of heat or mass transfer inside a droplet [44,47] have revealed that the transfer rate evolution is completely different to the external one: at a given Re_b , the Sherwood is bounded when increasing the Péclet number, and this asymptotic limit increases only very slightly when increasing Re_b in a large range. One interpretation of this effect involves the fact that when the recirculation motion, already containing solute, returns close to the bubble interface, it prevents the boundary layer around the bubble caps to be as small as it would be in an infinite medium for which the solute already transferred is convected far from the interface.

The evolution of Sh_{bs} with the Péclet number can be compared to the prediction of the model generally proposed for mass transfer around the bubble caps of a Taylor bubble, in the works of Irandoust et al. [3], van Baten and Krishna [9], Nirmal et al. [12] and Abiev [11]. The latter assume mass transfer along the caps to behave like around a spherical bubble rising in an unconfined liquid. In this way, they predict a local mass transfer coefficient based on the penetration model of Higbie [48], which is the dimensional form of the solution of Boussinesq [49] giving the Sherwood number to be proportional to $\sqrt{Pe_b} = \sqrt{|u_b|d/D}$ for both large Re_b and Pe_b (Figueroa-Espinoza and Legendre [45]). However, from fig. 13, it is clear that the evolution of Sh_{bs} as a function of Pe strongly differs from this scaling law. Such a discrepancy has never been reported in other works. This conclusion on Sh_{bs} is consistent with the local fluxes behaviour measured along the bubble caps in Section 4.2, where the contribution of the two caps in mass transfer were found to be comparable, which is in contrast to the case of an unconfined rising bubble. Thus, the evolution of Sh_{bs} as a function of $Pe^{1/2}$ is restricted to moderate Péclet numbers and, at higher Pe , the slower increase of Sh_{bs} should be taken into account in future models for mass transfer around the bubble caps of a Taylor bubble.

4.3.3. Exchange along the dividing streamline

The slug core is bounded by the dividing streamline of radial position r_1 , as illustrated in fig. 3. Fig. 14 presents several radial concentration profiles in the slug, for the case D at $Pe = 142$. At the rear of the bubble (line 1), the concentration is greater in the neighborhood of the convergent stagnation point. However, at a

short distance from the bubble rear (such as for line 2) and until the front of the following bubble, the maximum concentration values are observed at the channel wall, leading to an exchange flux of solute from the liquid film region towards the slug core. At large Pe , the thickness of this film is larger than that of the lubrication film along the bubble surface. From lines 2 to 4, this exchange flux decreases with the distance from the bubble rear because of the growth of the filament of dissolved oxygen along the wall.

In order to quantify this exchange flux and compare the different cases, rather than performing a surface integration of the radial flux along the dividing streamline to measure an average flux (which would be approximative to achieve since that streamline is not straight), the radial flux density $j_{ds} = -D \frac{\partial C}{\partial r}$ is evaluated at the boundary of the unit cell (along the line 3 in fig. 14) at $r = r_1$, taken as characteristic value. A local Sherwood number to characterise this exchange flux across the dividing streamline is then computed as $Sh_{ds,loc} = \frac{|j_{ds}|d}{D(\bar{C}_{film}(t) - \bar{C}_{slugcore}(t))}$, its value being retained when it is time independent. For all the simulation cases, fig. 15 plots $Sh_{ds,loc}$ as a function of a Péclet number $Pe_{ds} = \frac{w(r_1)d^2}{L_s D}$ describing the ratio between diffusion and convection time scales within the liquid slug. The convection time scale is based both on the liquid slug length and the axial velocity $w(r_1) = 2(|u_b| - |u_{rp}|)$ along the dividing streamline, given by eq. 8, which is directly proportional to the relative bubble velocity. The five experimental points from the study of Butler et al. [1], for which the same processing gives the normalised exchange flux density, are included in the plot. A single master curve well gathers the numerical points of $Sh_{ds,loc}$ from all cases, which confirms the importance of $w(r_1)$ (i.e. of the relative bubble velocity) for driving the mass exchange flux between the film region surrounding the slug core and the latter. Such a trend is observed to follow a $\sqrt{Pe_{ds}}$ function only over one decade range, corresponding to the highest Péclet number values in the simulations. The addition of the experimental points on this curve shows that such an evolution no longer continues at higher Pe_{ds} : the exchange flux still increases but at a smaller rate over several decades, leading to moderate Sherwood number values. An interpretation of such a saturation of this exchange flux could involve the same arguments as for the flux around the caps: the transfer being directed towards a region of closed streamlines (the slug core), the rate of transfer is completely different from the

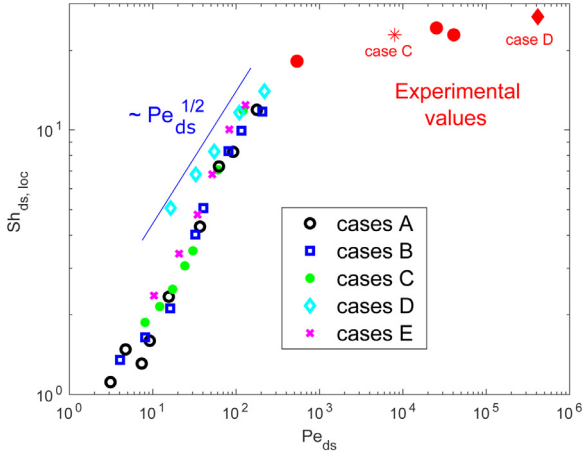


Fig. 15. For all cases, local Sherwood numbers characterising the normalised local exchange flux density between the liquid film region and the slug core, $Sh_{ds,loc}$, as a function of the Péclet number $Pe_{ds} = \frac{w(r_1)d_s^2}{L_s D}$ where $w(r_1)$ is the axial velocity at the dividing streamline position (note that $Pe_{ds} = 2Pe_R$ with Pe_R the Péclet number based on the relative bubble velocity). Red symbols: same data extracted from the experimental concentration fields measurements from Butler et al. [1] on five cases (including cases C and D of the present study, at higher Péclet numbers).

case of an unbounded region where convection is able to evacuate the transferred species far from the source of transfer. However, it can be noticed from figs. 13 and 15 that the saturation of this exchange flux appears for greater Péclet numbers than that of the simulations, i.e. a saturation of the flux coming from the bubble caps Sh_{bs} in terms of Pe is observed earlier.

4.4. Global Sherwood number

After the characterisation of the local transfer fluxes in the unit cell, a correlation for the global Sherwood number is proposed in this section. In this numerical study, five cases are considered with different bubble and two-phase velocities, different liquid phase systems, two contrasting channel diameters ($d = 3$ or 0.5 mm), different geometrical parameters of the bubble or unit cell (V_b , L_{uc} , L_b , L_s), with the numerical simulations allowing also the variation of D for a given case.

In the results presented in the previous sections, it was found that the Sherwood number globally decreases over time before settling on a constant value (fig. 7). After the steady regime of mass transfer is reached, it is straight-forward to verify that the profiles of flux along the interface can be obtained by homothetic scaling between two distinct times (see figs. 8 or 10). Moreover, at this stage, the concentration fields, $C(r, z, t)/\bar{C}(t)$, normalised by their instantaneous spatial average values, are found to remain identical (see figs. 5(c) and (d)). These arguments suggest that the concentration field $C(r, z, t)$ can be decomposed into a series of eigenmodes by separating the dependence in space and time. Then, as described by Rivero-Rodriguez and Scheid [50] for the case of trains of unconfined bubbles in microchannels, Sh_∞ is associated with the dynamics of the slowest mode of the solution and characterises the mass transfer process at long-time. In this section, we propose a scaling law to predict both Sh_∞ and the time required to reach this value.

In fig. 16(a), it is proposed to rationalise the computed values of Sh_∞ for the different cases by using a relative Péclet number $Pe_R = \frac{(|u_b| - |u_{tp}|) d^2}{L_s D}$, where the convection time scale in the slug is given by the global relative velocity $|u_b| - |u_{tp}|$ between the bubble and the average liquid flowing in the slug, with a length scale L_s , and the diffusion time scale given by d^2/D . The choice of this characteristic velocity is consistent with the one describ-

ing the exchange flux between the film region and the slug core, from Section 4.3.3. Fig. 16(a) shows that Sh_∞ presents an evolution which is proportional to $\sqrt{Pe_R}$, for each case (actually, on this sub-figure (a), for a given case, only D is varied). But such a plot presents the interest that the proportionality constants of the different cases can be ordered depending on the volume fraction of gas in the unit cell, V_b/V_{uc} : a lower gas volume fraction always results in a greater Sh_∞ , at a given Pe_R . Taking into account this observation, the global Sherwood numbers are grouped together by considering the following correlation, proposed in fig. 16(b), of the form:

$$Sh_\infty = 0.522 \sqrt{Pe_R} (V_b/V_{uc})^{-1.65} \quad (26)$$

The scaling law eq. 26 is based on the two non-dimensional parameters Pe_R and V_b/V_{uc} , and a prefactor of order 1. The figure shows that the results from the numerical simulations collapse on a master curve with excellent accuracy, across two orders of magnitude. Therefore, the proposed correlation constitutes an accurate description of the global mass transfer rate over the range of investigated parameters, for $Pe_R \leq 100$ and V_b/V_{uc} varied between 24 and 48% in the simulations.

The scaling proposed for Sh_∞ in eq. 26 is valid provided that steady state is reached. From the simulations, the time t_∞ required to reach such a regime is defined as the time where the moving average of the curve $Sh(t)$, measured over time t_{cir} , becomes equal to $Sh_\infty \pm 1\%$. The measured times t_∞/t_{cir} are presented in fig. 17 as a function of the Péclet number Pe . This figure can be used to determine the residence time, i.e. the channel length at a given flow rate, that is required to reach the steady regime. This time increases with Pe but, from values $Pe > 100$, there is a clear change in behaviour. This can be related to the time evolution of Sh , which differs at high Pe as shown by fig. 7: when $Pe > 100$, the curve $Sh(t)$ presents a slow initial decrease with oscillations at higher frequency $1/t_{cir}$, whereas, at lower Pe , the initial decrease is much stronger and the instantaneous values of Sh can even be smaller than Sh_∞ before rapidly stabilising. In fig. 17, a correlation is proposed to predict the time t_∞ for large Pe based on the simulation results, of the form:

$$t_\infty = 0.01 t_{diff}, \quad (27)$$

established for $100 \leq Pe \leq 1000$.

4.5. Discussion with experimental data

In the study of Butler et al. [1], the experimental concentration fields have revealed the presence of some unusual patterns of high concentrations of solute dispersed inside zones of lower concentrations in the slug core (see the experimental pictures of cases A, B, D on fig. 2). This phenomenon, discussed in Abiev et al. [51], could be due to initial effects during the bubble formation stage (see also the concentration field during this stage from Liu et al. [52]). Since the initial conditions are different in the simulations, as well as the range of Péclet number, the experimental and numerical concentration fields cannot be directly compared. However, a comparison could be achieved through the scaling law evolution of Sh_∞ obtained from the numerical results. The first step is to assess the influence of the initial distribution of concentration in the slug on the long-term transfer dynamics, before comparing the numerical and experimental Sherwood number evolutions.

4.5.1. Influence of initial conditions

In experimental studies, the mass transfer taking place close to the contact zone between the gas and liquid phases, before the full establishment of the Taylor flow, can be significant [53]. To address the question of the influence of the first stages of mass transfer on

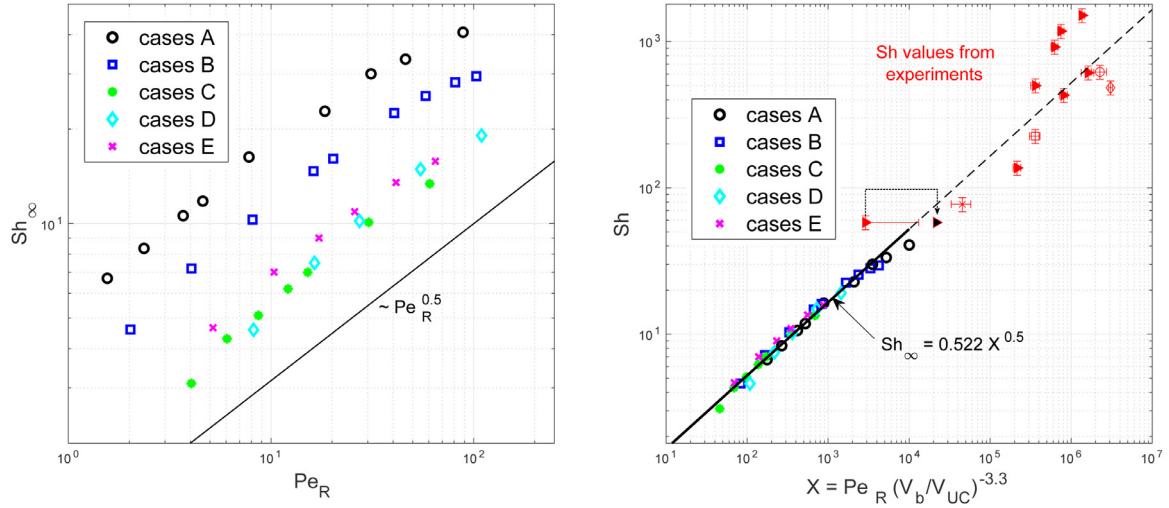


Fig. 16. (a) Sh_∞ as a function of $Pe_R = \frac{(|u_b| - |u_{pl}|) d^2}{L_r D}$ for the different simulation cases. (b) Proposed scaling law from eq. 26. The plot includes all numerical data from this study (Sh_∞) and experimental points (global Sh) from Butler et al. [1] where the mass transfer coefficient is taken as defined by eq. 17. The experimental points have been obtained at larger Pe_R and may not all correspond to Sh_∞ since a constant value of Sh is probably reached only for the two cases of lower Pe_R (based on estimates of the time required to reach the steady regime), as discussed in the Section 4.5.2. Note that the abscissa of one experimental point has been shifted by using a value of $|u_{pl}|$ obtained from a simulation of the hydrodynamics in this case because of the large experimental uncertainty on this value.

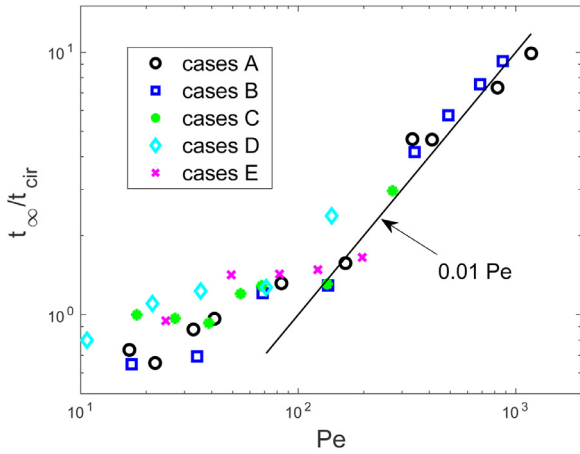


Fig. 17. For all cases, normalised time t_∞/t_{cir} required to reach the steady regime of transfer (defined by $Sh = Sh_\infty \pm 1\%$), as a function of Pe .

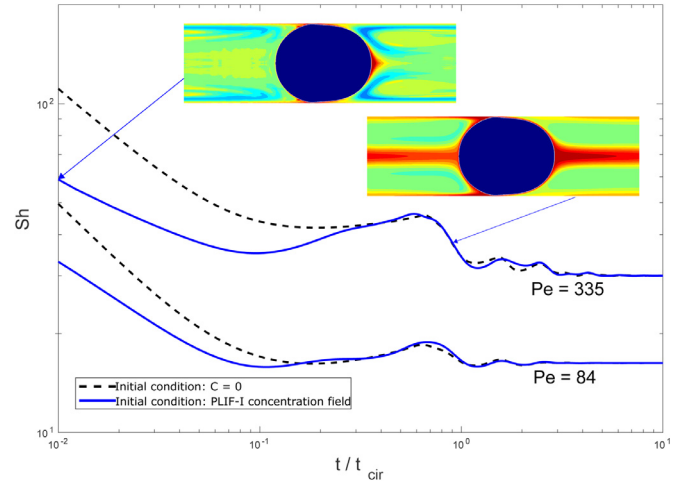


Fig. 18. For case A, time evolution of the Sherwood number in a simulation where an instantaneous concentration field measured by the PLIF-I technique from Butler et al. [1] is used to initialise the simulation (continuous lines), versus the solution otherwise obtained with a zero initial concentration field (dashed lines), for the conditions $Pe = 84$ and 335 . The screenshots display the concentration field at two instants ($t=0$ and $0.9 t_{cir}$) for $Pe = 335$.

the long-term dynamics, simulations were performed by using different initial conditions in the liquid. For case A, a concentration field in the liquid phase, directly taken from the PLIF-I experimental study of Butler et al. [1] at the first position of measurement along the experimental channel (already far from the injection, at a distance of $198d$), is used to initialise new simulations of mass transfer at $Pe = 84$ and 335 , by conserving the same converged hydrodynamics and bubble shape as before. To this purpose, the experimental concentration field in the liquid, recorded on a pixel grid, has been interpolated to the numerical mesh grid so as to be used as initial condition; the latter is shown in fig. 18, and also corresponds to the field presented in fig. 9 of [1].

In fig. 18, the time evolution of the Sherwood number for these simulations is compared to that of the same cases where there is initially no solute in the liquid phase. Some differences are noticeable at short time: since the beginning, the values of Sh with the experimental concentration field are closer to their long-term values, the time evolution of Sh presenting a lower rate of decrease compared to the case starting from a null concentration which requires a longer time to establish the mass boundary layer around the interface. However, after the different transient stages for the

two initial conditions, the evolution of Sh is no longer affected by the initial conditions, leading to the same Sh_∞ . This conclusion is consistent with the fact that Sh_∞ is a parameter characteristic of the long-time behaviour of mass transfer [50], allowing comparisons when the constant Sh condition is achieved.

4.5.2. Comparison of the global Sherwood numbers

In the experiments from Butler et al. [1], the Péclet numbers are much higher than in the simulations and lie in the range $12,000 \leq Pe \leq 340,000$. Fig. 16(b) compares the experimental Sherwood numbers with an extrapolation of the numerical correlation eq. 26. It can be seen that the experimental values are consistent with the numerical correlation and are distributed around the predicted values. Nevertheless, it is worth reminding the conditions of measurement of the experimental Sherwood numbers. As what is conventionally done, in Butler et al. [1], the mass transfer coefficient for each case was obtained from fitting of the curve of the four

measurement points of the average liquid concentration \bar{C}/C^* by a $\exp(-k_l a t)$ function. However, it has been shown here that such a fitting function is only valid for long times, once the steady regime of transfer is reached, i.e. under measurement times of the order of t_∞ . Therefore, even though these global experimental Sherwood numbers are suitable to describe the average transfer rate during the time of residence considered (not the same for all experimental conditions), they may not all correspond to Sh_∞ values as defined in the simulations.

By using eq. 27 to predict t_∞ , it is estimated that only the experimental cases at the two lower Péclet numbers may have reached the steady regime of mass transfer (corresponding to the experimental points at the lower abscissa on fig. 16(b)). Note that, concerning the first of these points (regime 1 in Butler et al. [1]) and contrary to the other points, the uncertainty on the measured u_{tp} was relatively high compared to the velocity difference $u_b - u_{tp}$, impacting strongly the value of the relative Péclet number Pe_R used in the correlation. Then, to increase the accuracy of this point, the hydrodynamics of this case has been simulated: u_{tp} is found to differ by only 6% in the simulation compared to the measured value, which permits to estimate a better abscissa for this point on fig. 16(b), in agreement with the error bar estimated in the measurements.

By considering that the two experimental values at the lower Pe are Sh_∞ values, it can be seen in fig. 16(b) that they are close to the prediction from the extrapolated correlation, by being lower of about 30%. For the remaining cases, Sh_∞ can be expected to be smaller than the measured Sh since $Sh(t)$ is globally a decreasing function of time during the transient. Then, by combining all these numerical and experimental results, it can be reasonably inferred that, at higher Péclet numbers than in the simulations ($Pe_R > 100$), the increase of Sh_∞ with Pe_R would take place at smaller rate than as a $\sqrt{Pe_R}$ evolution. Such an observation on the global rate of transfer in the unit cell could not be surprising, considering the conclusions already obtained on (i) a saturation of the Sherwood number Sh_{bs} characterising mass transfer around the bubble caps, visible at the higher Péclet number values in the simulation cases, and (ii) the smaller rate of increase of $Sh_{ds,loc}$ exhibited at the experimental Péclet number values concerning the mass exchange between the film and slug region. Obviously, this conclusion on the evolution of Sh_∞ as a function of Pe_R would need to be validated by simulations at much higher Péclet numbers or by experimental results fulfilling the condition of having reached a steady regime of mass transfer.

5. Conclusions

In this study, five trains of axisymmetric Taylor bubbles flowing in channels have been simulated using the unit cell periodic approach, based on the Level-Set method. These cases, originating mainly from a previous experimental study and another numerical study, present a variety of different geometrical parameters (unit cells, bubbles), and sit within the inertial regime, having bubble Reynolds numbers between 200 and 700 with moderate-to-high Weber numbers. The hydrodynamics features (such as the two-phase velocity, lubrication film thickness and bubble shape) were found to be in good agreement with existing results.

On this basis, simulations of the mass transfer dynamics have been performed using the converged hydrodynamic fields by varying the diffusion coefficients in a range of Péclet numbers $10 \leq Pe \leq 900$. High spatial resolution has been required to accurately solve the thin mass boundary layers that develop around the bubble interface. The analysis of the local transfer fluxes has revealed that the highest gradients are located (i) at the bubble front, close to the divergent stagnation point (corresponding to the entrance of the film) and (ii) at the bubble rear, at the point where the tan-

gential velocity of the fluid is the highest. High temporal resolution allows for the observation of the oscillation of the global Sherwood number evolution, at a period determined by the circulation time t_{cir} , and makes it possible to show that an unsteady regime takes place during which the different local transfer processes develop. They are namely the fast convective processes along both the channel axis and the dividing streamline, diffusion across the boundary layers around the bubble caps and in the lubrication film, and a mass exchange process from the film along the wall towards the slug core region. During this transient period, the Sherwood number decreases over time before reaching a constant value Sh_∞ . The number of circulations required to reach this steady regime increases with Pe . Afterwards, the average concentration in the liquid phase grows based on a $\exp(-k_l a t)$ function, in agreement with the models which assume a perfectly mixed liquid phase: such a function with constant mass transfer coefficient is therefore suitable for describing the long-time evolution of the liquid concentration.

In the steady regime, in the film zone of the bubble interface, the transfer flux follows an evolution $Sh_{bf} \sim Pe_{film}^{1/2}$ provided Pe_{film} is greater than 1, as predicted analytically by a balance between axial convection and radial diffusion. The excellent agreement of this analytical model with the simulation results allows being confident to use it to predict an accurate value for the transfer coefficient across the interface in contact with the lubrication film.

After being enriched by contact with the bubble surface, the liquid film continues flowing along the wall (in the bubble frame) and mainly discharges the solute into the core of the slug, at a rate Sh_{exch} which increases with the Péclet number Pe_{ds} . However, the increase of this transfer rate becomes smaller at Pe_{ds} greater than 1,000. This exchange flux contributes to enrich the outermost streamline of the slug core region, in addition to the transfer flux coming from the two bubble caps. The latter is quantified by Sh_{bs} , and evolves as $\sim Pe^{1/2}$ only at moderate Péclet numbers ($Pe < 100$), contrary to what is generally assumed in the models which use correlations for mass transfer around a freely rising bubble to characterise mass transfer around the bubble caps. The simulations performed here prove that at large Pe , Sh_{bs} increases slower than a $Pe^{1/2}$ evolution: this is characteristic of a mass transfer process in a region of closed streamlines, completely different from transfer towards an unbounded region.

Such local characterisations of the local transfer processes in Taylor flows have never been reported or verified in previous studies, and will be useful for local models of mass transfer distinguishing the contribution from the different zones.

As the different Taylor flows investigated here show common features on the local mass transfer dynamics, a common correlation to predict the global Sh_∞ has been proposed, eq. 26, which gathers all the numerical results. This correlation gives Sh_∞ as an increasing function of both a Péclet number Pe_R , based on the relative slip velocity, and of the volume fraction of the liquid phase in the unit cell. The scaling law covers two orders of magnitude of Pe_R (until 100), and involves several hydrodynamic and geometrical parameters. Then, it constitutes a reference for a comparison with experimental Sherwood numbers from Butler et al. [1], at cases of higher Péclet numbers ($Pe_R \geq 2,000$). Such a comparison is challenging because of the completely different values of physical parameters involved (Pe_R , Reynolds and Weber numbers, geometrical ratios), the possible influence of residual impurities in experiments and different initial conditions for the hydrodynamics and the mass transfer (than in the simulations) as injection effects are present in the experiments and create particular concentration patterns at the contact point between the gas and liquid phase. Thanks to simulations initialised with experimental concentration fields, it has been possible to show that initial conditions do not modify the long-term transfer dynamics measured by Sh_∞ ,

which is therefore a robust parameter for a comparison, provided the time t_∞ required to reach the steady regime of mass transfer is reached. Considering the experimental cases at the lowest Pe_R where the latter condition is probably satisfied, the experimental values of Sh_∞ are close to the predictions by the numerical correlation and tend to show that Sh_∞ could increase at a smaller rate than a $\sqrt{Pe_R}$ evolution at $Pe_R > 100$. Such a conclusion should be confirmed in further works.

This study constitutes an example of the strong complementarity between numerical and experimental studies, permitting a detailed understanding of the transfer mechanisms (mass or heat transfer) involved within a train of Taylor bubbles.

Disclosure of conflicts of interest

The authors declare that they have no known competing financial interests or personal relationships that could have appeared to influence the work reported in this paper.

Declaration of Competing Interest

The authors declare that they have no known competing financial interests or personal relationships that could have appeared to influence the work reported in this paper.

Appendix A

This appendix presents two validation cases on the problem of mass transfer around (i) a static bubble and (ii) a rising bubble in a large range of Péclet numbers Pe_b .

Mass transfer in the pure diffusive regime

A static spherical bubble of radius R is considered, which is assumed to have uniform concentration, the interface being at a concentration $C(r = R, t) = C^*$ and the external liquid (at rest) at a concentration $C(r \rightarrow \infty, t) = C_i = 0$ at an infinite distance from the bubble. The transient mass transfer process, only due to diffusion, is solved in the liquid phase, starting from zero concentration at initial time in the liquid phase ($C(r, 0) = C_i = 0$ for $r > R$). The radial concentration profile at several time instants can then be compared with the analytical solution of the problem [54], given by

$$C(r, t) = C^* - \frac{1}{r} \frac{C^* - C_i}{2\sqrt{\pi Dt}} \int_0^\infty (R + \xi') \left\{ \exp\left[-\frac{(\xi - \xi')^2}{4Dt}\right] - \exp\left[-\frac{(\xi + \xi')^2}{4Dt}\right] \right\} d\xi' \quad (28)$$

where $\xi = r - R$. As can be clearly seen in [fig. A.19](#), there is excellent agreement between the numerical and analytical solution for all times, for this purely diffusive case.

Mass transfer around a rising bubble

The mass transfer around a spherical bubble rising in an external liquid at rest is considered, for a Reynolds number of 20, for a sufficiently low Bond number so there is no deformation of the interface, and for varying Schmidt numbers, leading to a large range of Péclet numbers $Pe_b = \frac{u_b d}{D}$. Hydrodynamics are solved until steady state for the rising motion; then, based on this converged velocity field, the transient mass transfer process is simulated with the same boundary and initial conditions as in the previous validation case. Simulations are axisymmetric and performed on different grids from 10 to 240 nodes per bubble radius.

Physical values of the different properties used for the simulation can be found in the caption of [Table 5](#). Based on the value

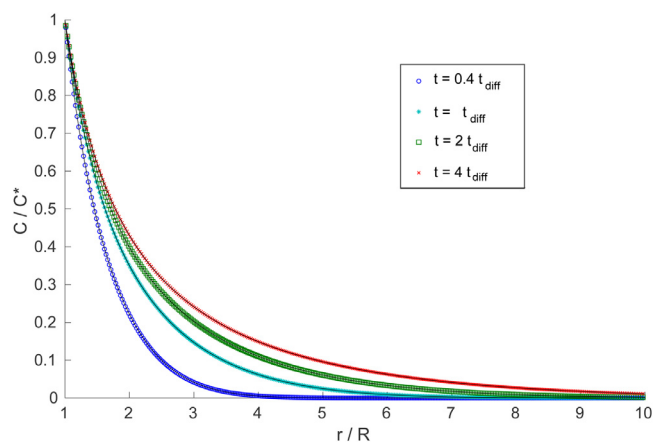


Fig. A1. Validation case - Mass transfer around a spherical bubble in the pure diffusion regime. Comparison of the simulation profiles (symbols) to the analytical solution eq. 28 (continuous lines) at four different times, expressed as a function of the diffusive time $t_{diff} = d^2/D$.

of the drag coefficient from the boundary-fitted simulations of Oliver and Chung [55], the Reynolds number at steady state should be equal to $Re_b = 20$ in an unconfined media. The comparison of results of terminal velocity presented in [Table 5](#) show excellent agreement, with a discrepancy of only -3%, as well as demonstrating clear mesh convergence. This small discrepancy is attributed to the slight confinement imposed by the size of the simulation box, which is of (8R, 16R). Hydrodynamics around the bubble is then considered to be well computed by the code.

For the mass transfer simulations, the Sherwood number defined by

$$Sh_\infty = \frac{-\int_b \nabla C \cdot \mathbf{n} dS}{C^* S_b} d, \quad (29)$$

is calculated when it has reached a constant value. The latter is compared with the correlation proposed by Colombet et al. [44] from boundary-fitted simulations, given by

$$Sh_{\infty, pred} = 1 + \left[1 + \left(\frac{4}{3\pi} \right)^{2/3} (2Pe_{max})^{2/3} \right]^{3/4}, \quad (30)$$

where $Pe_{max} = \frac{u_{max} d}{D}$ is based on the maximum tangential velocity at the interface, given by the relation proposed by Legendre [56] as

$$u_{max} = \frac{1}{2} \frac{16 + 3.315Re_b^{1/2} + 3Re_b}{16 + 3.315Re_b^{1/2} + Re_b} u_b \quad (31)$$

The results are summarised in [Table 5](#) for a large range of Péclet numbers. The mesh convergence of the results are clearly illustrated, noting that achieving a lower discrepancy for Sh is more demanding than for the hydrodynamics, at large Pe_b . Indeed, it is observed that when the mass transfer boundary layer is not resolved enough, the concentration gradient in the normal direction to the interface, i.e the mass transfer flux, is underestimated, whereas the level of error for the simulation falls drastically when the mesh resolution becomes sufficient. It can therefore be concluded that the meshes used for this benchmark allow for the accurate simulation of the mass transfer dynamics until $Pe_b = 10,000$ with an error less than 3%, noting that the boundary layer is captured on four grid cells at its thinnest part at $Pe_b = 10,000$ with a mesh resolution of 240 nodes per bubble radius.

Appendix B

In [Table 6](#), the mesh sensitivity analysis carried out on the computation of the mass transfer rate in the considered Taylor flows

Table 5

Validation case - Sherwood number in the steady regime around a spherical freely bubble rising for $Re_b = \frac{\rho_l u_b d}{\mu_l} = 20$, $Bo = \frac{(\rho_l - \rho_g)gd^2}{\sigma} = 0.025$ (theoretical prediction, eq. 30) and at different Pe_b numbers. Six numerical grids are used. Physical parameters: $d = 39.1 \mu\text{m}$, $\rho_l = 1.000 \text{ kg/m}^3$, $\mu_l = 0.00113 \text{ Pa}\cdot\text{s}$, $\rho_g = 1.226 \text{ kg/m}^3$, $\mu_g = 1.78 \times 10^{-5} \text{ Pa}\cdot\text{s}$, $g = -9, 144.4 \text{ m/s}^2$, $\sigma = 0.56 \text{ N/m}$, D is varied from 2.3×10^{-9} to $1.1 \times 10^{-7} \text{ m}^2/\text{s}$ so as to produce different Péclet numbers.

Number of mesh points per radius	10	20	40	80	120	240
Discrepancy on Re_b	1.4%	-0.6%	-4.5%	-3.9%	-3.2%	-3.0%
Discrepancy on Sh_∞ at $Pe_b = 200$	-49.4%	-8.86%	1.2%	0.5%	-0.3%	-0.1%
Discrepancy on Sh_∞ at $Pe_b = 1,000$		-53.2%	-18.7%	2.3%	3.5%	1.4%
Discrepancy on Sh_∞ at $Pe_b = 2,000$		-72.6%	-37.2%	-4.7%	2.4%	1.3%
Discrepancy on Sh_∞ at $Pe_b = 5,000$				-24.2%	0.6%	-0.1%
Discrepancy on Sh_∞ at $Pe_b = 10,000$				-42.8%	-8.5%	3.3%

Table 6

Sensitivity of Sherwood number Sh_∞ obtained after simulations of cases A-E by using different grids. Δx is the characteristic mesh size around the interface.

Case A	Mesh grid	337 × 780	457 × 1340	670 × 1850
	Δx @ interface	5 μm	3.3 μm	2.2 μm
	$Pe = 84$	-	$Sh_\infty = 16.3$	$Sh_\infty = 16.4$
	$Pe = 419$	-	$Sh_\infty = 32.3$	$Sh_\infty = 33.4$
	$Pe = 838$	$Sh_\infty = 35.5$	$Sh_\infty = 38.0$	$Sh_\infty = 48.1$
Case B	Mesh grid	256 × 1900	400 × 2100	600 × 3150
	Δx @ interface	5.9 μm	3.8 μm	2.5 μm
	$Pe = 343$	$Sh_\infty = 22.5$	$Sh_\infty = 22.5$	$Sh_\infty = 22.1$
	$Pe = 686$	-	$Sh_\infty = 28.2$	$Sh_\infty = 27.9$
Case C	Mesh grid	74 × 680	400 × 2100	
	Δx @ interface	24.9 μm	6.8 μm	
	$Pe = 54$	$Sh_\infty = 5.4$	$Sh_\infty = 6.2$	
	$Pe = 272$	$Sh_\infty = 11.5$	$Sh_\infty = 13.6$	
Case D	Mesh grid	190 × 1080	380 × 2200	
	Δx @ interface	8.1 μm	4.0 μm	
	$Pe = 21$	$Sh_\infty = 6.5$	$Sh_\infty = 7.5$	
	$Pe = 36$	$Sh_\infty = 8.7$	$Sh_\infty = 10.5$	
	$Pe = 71$	$Sh_\infty = 12.1$	$Sh_\infty = 14.9$	
Case E	Mesh grid	80 × 528	160 × 1056	
	Δx @ interface	3.1 μm	1.6 μm	
	$Pe = 49$	$Sh_\infty = 6.9$	$Sh_\infty = 7.0$	
	$Pe = 81$	$Sh_\infty = 8.8$	$Sh_\infty = 9.0$	
	$Pe = 122$	$Sh_\infty = 10.6$	$Sh_\infty = 10.9$	

of Table 2 is detailed, for cases A-E. It can be seen that, in the range of investigated Péclet numbers, the Sh_∞ values are very close when increasing the level of refinement of the grid, thus validating the reliability of the results for the physical analysis presented in Section 4. Such tests allows for determining the highest Péclet number condition for mass transfer which can accurately be simulated on a given mesh.

CRedit authorship contribution statement

Colin Butler: Conceptualization, Methodology, Software, Validation, Investigation, Data curation, Writing – review & editing. **Emmanuel Cid:** Conceptualization, Data curation, Visualization, Writing – review & editing, Funding acquisition. **Anne-Marie Billet:** Conceptualization, Supervision, Writing – review & editing, Project administration, Funding acquisition. **Benjamin Lalanne:** Conceptualization, Methodology, Software, Investigation, Writing – original draft, Writing – review & editing, Supervision, Project administration, Funding acquisition.

References

[1] C. Butler, B. Lalanne, K. Sandmann, E. Cid, A.M. Billet, Mass transfer in taylor flow: transfer rate modelling from measurements at the slug and film scale, *Int J Multiph Flow* 105 (2018) 185–201.

[2] M.T. Kreutzer, F. Kapteijn, J.A. Moulijn, J.J. Heiszwolf, Multiphase monolith reactors: chemical reaction engineering of segmented flow in microchannels, *Chem Eng Sci* 60 (22) (2005) 5895–5916.

[3] S. Irandoust, S. Ertlé, B. Andersson, Gas-liquid mass transfer in taylor flow through a capillary, *Can J Chem Eng* 70 (1992) 115–119.

[4] G. Berčič, A. Pintar, The role of gas bubbles and liquid slug lengths on mass transport in the taylor flow through capillaries, *Chem Eng Sci* 52 (21) (1997) 3709–3719.

[5] C.O. Vandu, H. Liu, R. Krishna, Mass transfer from taylor bubbles rising in single capillaries, *Chem Eng Sci* 60 (22) (2005) 6430–6437.

[6] J. Yue, Q. Yuan, L. Luo, Y. Gonthier, Hydrodynamics and mass transfer characteristics in gas-liquid flow through a rectangular microchannel, *Chem Eng Sci* 62 (7) (2007) 2096–2108.

[7] N. Dietrich, K. Loubière, M. Jimenez, G. Hébrard, C. Gourdon, A new direct technique for visualizing and measuring gas-liquid mass transfer around bubbles moving in a straight millimetric square channel, *Chem Eng Sci* 100 (2013) 172–182.

[8] C. Butler, E. Cid, A.M. Billet, Modelling of mass transfer in taylor flow: investigation with the PLIF-i technique, *Chem Eng Res Des* 115 (2016) 292–302.

[9] J.M. van Baten, R. Krishna, CFD Simulations of mass transfer from taylor bubbles rising in circular capillaries, *Chem Eng Sci* 59 (12) (2004) 2535–2545.

[10] R.S. Abiev, Bubbles velocity, taylor circulation rate and mass transfer model for slug flow in milli- and microchannels, *Chem Eng J* 227 (2013) 66–79.

[11] R.S. Abiev, Gas-liquid and gas-liquid-solid mass transfer model for taylor flow in micro (milli) channels: a theoretical approach and experimental proof, *Chem Eng J Advances* 4 (2020) 100065.

[12] G.M. Nirmal, T.F. Leary, A. Ramachandran, Mass transfer dynamics in the dissolution of taylor bubbles, *Soft Matter* 15 (13) (2019) 2746–2756.

[13] F. Xu, G. Hébrard, N. Dietrich, Comparison of three different techniques for gas-liquid mass transfer visualization, *Int J Heat Mass Transf* 150 (2020) 119261.

[14] M. Mei, G. Hébrard, N. Dietrich, K. Loubière, Gas-liquid mass transfer around taylor bubbles flowing in a long, in-plane, spiral-shaped milli-reactor, *Chem Eng Sci* 222 (2020) 115717.

[15] N. Shao, A. Gavriilidis, P. Angeli, Mass transfer during taylor flow in microchannels with and without chemical reaction, *Chem Eng Sci* 160 (3) (2010) 873–881.

[16] R. Gupta, D.F. Fletcher, B.S. Haynes, Cfd modelling of flow and heat transfer in the taylor flow regime, *Chem Eng Sci* 65 (6) (2010) 2094–2107.

[17] C.J. Falconi, C. Lehrenfeld, H. Marschall, C. Meyer, R. Abiev, D. Bothe, A. Reusken, Numerical and experimental analysis of local flow phenomena in laminar taylor flow in a square mini-channel, *Phys Fluids* 28 (1) (2016) 012109.

[18] R. Gupta, D.F. Fletcher, B.S. Haynes, On the CFD modelling of taylor flow in microchannels, *Chem Eng Sci* 64 (12) (2009) 2941–2950.

[19] D.F. Fletcher, B.S. Hayes, Cfd simulation of taylor flow: should the liquid film be captured or not? *Chem Eng Sci* 167 (2017) 334–335.

[20] F.L. Durán Martínez, C. Julcour-Lebigue, A.M. Billet, F. Larachi, Modelling and simulations of a monolith reactor for three-phase hydrogenation reactions - rules and recommendations for mass transfer analysis, *Catal Today* 273 (2016) 121–130.

[21] P. Albrand, C. Julcour, V. Gerbaud, A.M. Billet, Accurate hydrogenated vegetable oil viscosity predictions for monolith reactor simulations, *Chem Eng Sci* 214 (2020) 115388.

[22] M.C. Silva, J.M. Miranda, J.B. Campos, J.D. Araújo, Mass transfer from a taylor bubble to the surrounding flowing liquid at the micro-scale: a numerical approach, *Microfluid Nanofluid* 23 (4) (2019) 58.

[23] A. Hassanvand, S.H. Hashemabadi, Direct numerical simulation of mass transfer from taylor bubble flow through a circular capillary, *Int J Heat Mass Tran* 55 (2012) 5959–5971.

- [24] L. Yang, M.J. Nieves-Remacha, K.F. Jensen, Simulations and analysis of multi-phase transport and reaction in segmented flow microreactors, *Chem Eng Sci* 169 (2017) 106–116.
- [25] K. Hayashi, A. Tomiyama, Effects of surfactants on terminal velocity of a Taylor bubble in a vertical pipe, *Int J Multiphase Flow* 39 (2012) 78–87.
- [26] T. Abadie, J. Aubin, D. Legendre, On the combined effects of surface tension force calculation and interface advection on spurious currents within volume of fluid and level set frameworks, *J Comp Phys* 297 (2015) 611–636.
- [27] A. Kuzmin, M. Januszewski, D. Eskin, F. Mostowfi, J.J. Derksen, Lattice Boltzmann study of mass transfer for two-dimensional Bretherton/Taylor bubble train flow, *Chem Eng J* 225 (2013) 580–596.
- [28] K. Hayashi, S. Hosoda, G. Tryggvason, A. Tomiyama, Effects of shape oscillation on mass transfer from a Taylor bubble, *Int J Multiphase Flow* 58 (2014) 236–245.
- [29] H. Marschall, S. Boden, C. Lehrenfeld, U. Hampel, A. Reusken, M. Wörner, D. Bother, Validation of interface capturing and tracking techniques with different surface tension treatments against a Taylor bubble benchmark problem, *Comput Fluids* 102 (2014) 336–352.
- [30] B. Lalanne, L. Rueda-Villegas, S. Tanguy, F. Risso, On the computation of viscous terms for incompressible two-phase flows with level set/ghost fluid method, *J Comp Phys* 301 (2015) 289–307.
- [31] L. Rueda-Villegas, R. Alis, M. Lepilliez, S. Tanguy, A ghost fluid/level set method for boiling flows and liquid evaporation: application to the Leidenfrost effect, *J Comp Phys* 316 (2016) 789–813.
- [32] F. Gibou, R.P. Fedkiw, L.T. Cheng, M. Kang, A second-order-accurate symmetric discretization of the Poisson equation on irregular grids, *J Comp Phys* 176 (1) (2002) 205–227.
- [33] T. Aslam, A partial differential equation approach to multidimensional extrapolation, *J Comput Physics* 193 (2003) 349–355.
- [34] S. Tanguy, T. Ménard, A. Berlemont, A level set method for vaporizing two-phase flows, *J Comp Phys* 221 (2) (2007) 837–853.
- [35] S. Tanguy, M. Sagan, B. Lalanne, F. Couderc, C. Colin, Benchmarks and numerical methods for the simulation of boiling flows, *J Comp Phys* 264 (2014) 1–22.
- [36] G. Huber, S. Tanguy, M. Sagan, C. Colin, Direct numerical simulation of nucleate pool boiling at large microscopic contact angle and moderate Jakob number, *Int J Heat Mass Transf* 113 (2017) 662–682.
- [37] A. Orazzo, S. Tanguy, Direct numerical simulations of droplet condensation, *Int J Heat Mass Transf* 129 (2019) 432–448.
- [38] G.I. Taylor, Deposition of a viscous fluid on the wall of a tube, *J Fluid Mech* 10 (2) (1961) 161–165.
- [39] T.C. Thulasidas, M.A. Abraham, L.R. Cerro, Flow patterns in liquid slugs during bubble-train flow inside capillaries, *Chem Eng Sci* 52 (17) (1997) 2947–2962.
- [40] P. Aussillous, D. Quéré, Quick deposition of a fluid on the wall of a tube, *Phys Fluids* 12 (10) (2000) 2367–2371.
- [41] Y. Han, N. Shikazono, Measurement of the liquid film thickness in micro tube slug flow, *Int J Heat Fluid Flow* 30 (5) (2009) 842–853.
- [42] R.S. Abiev, Simulation of the slug flow of a gas-liquid system in capillaries, *Theor Found Chem Eng* 42 (2) (2008) 105–117.
- [43] J. Zhang, X. Li, X. Wang, B. Sundén, B.Z. Wu, Numerical studies of gas-liquid Taylor flows in vertical capillaries using CuO/water nanofluids, *Int Commun Heat Mass* 116 (2020) 104665.
- [44] D. Colombet, D. Legendre, A. Cockx, P. Guiraud, Mass or heat transfer inside a spherical gas bubble at low to moderate Reynolds number, *Int J Heat Mass Transf* 67 (2013) 1096–1105.
- [45] B. Figueroa-Espinoza, D. Legendre, Mass or heat transfer from spheroidal gas bubbles rising through a stationary liquid, *Chem Eng Sci* 65 (23) (2010) 6296–6309.
- [46] D. Eskin, F. Mostowfi, A model of a bubble train flow accompanied with mass transfer through a long microchannel, *Int J Heat Fluid Flow* 33 (1) (2012) 147–155.
- [47] G. Juncu, A numerical study of the unsteady heat/mass transfer inside a circulating sphere, *Int J Heat Mass Transf* 53 (15–16) (2010) 3006–3012.
- [48] R. Higbie, The rate of absorption of a pure gas into a still liquid during short periods of exposure, *Trans A.I.Ch.E.* 31 (1935) 365–389.
- [49] J. Boussinesq, Calcul du pouvoir refroidissant des courants fluides, *Math Pure Appl* 60 (1905) 285–332.
- [50] B. Rivero-Rodríguez, B. Scheid, Mass transfer around bubbles flowing in cylindrical microchannels, *J Fluid Mech* 869 (2019) 110–142.
- [51] R.S. Abiev, C. Butler, E. Cid, B. Lalanne, A.M. Billet, Mass transfer characteristics and concentration field evolution for gas-liquid Taylor flow in milli channels, *Chem Eng Sci* 207 (2019) 1331–1340.
- [52] Y. Liu, Q. Zhao, J. Yue, C. Yao, G. Chen, Effect of mixing on mass transfer characterization in continuous slugs and dispersed droplets in biphasic slug flow microreactors, *Chem Eng Sci* 406 (2021) 126885.
- [53] L. Yang, N. Dietrich, K. Loubière, C. Gourdon, G. Hébrard, Visualization and characterization of gas liquid mass transfer around a Taylor bubble right after the formation stage in microreactors, *Chem Eng Sci* 143 (2016) 364–368.
- [54] H.S. Carslaw, Introduction to the mathematical theory of the conduction of heat in solids, Dover Publications, New York, 1945.
- [55] D.L.R. Oliver, J.N. Chung, Flow about a fluid sphere at low and moderate Reynolds numbers, *J Fluid Mechanics* 177 (1987) 1–18.
- [56] D. Legendre, On the relation between the drag and the vorticity produced on a clean bubble, *Phys Fluids* 19 (1) (2007) 018102.